geosciences

MDPI

Article

Geological and Geochemical Characterization of Variscan Pegmatites in the Sidi Bou Othmane District, Central Jebilet Province, Morocco

Amina Wafik [1], Nouamane El Aouad [1,2], Youssef Daafi [3], Yousra Morsli [4], Marouane Chniouar [1], Rosalda Punturo [5,6], Aida Maria Conte [6], Daniela Guglietta [6,*] and Wissale Aba Sidi [1,2]

[1] DLGR Laboratory, Faculty of Sciences Semlalia, Cadi Ayyad University, Marrakech 40000, Morocco; wafik@uca.ac.ma (A.W.); nouaman.geomine@gmail.com (N.E.A.); marouanechniouar@gmail.com (M.C.); abasidiwissale1@gmail.com (W.A.S.)
[2] Applied Geophysics, Water and Environment Laboratory, Faculty of Sciences and Technics, Sultan Moulay Slimane University, Béni Mellal 23000, Morocco
[3] OCP Group, Bd Moulay Youssef, Youssoufia 46300, Morocco; daafi@ocpgroup.ma
[4] Geosciences and Applications Laboratory, Faculty of Sciences Ben Msik, Casablanca 20670, Morocco; yousramorsli@gmail.com
[5] Department of Biological, Geological and Environmental Sciences, University of Catania, 95124 Catania, Italy; rosalda.punturo@unict.it
[6] Institute of Environmental Geology and Geoengineering, National Research Council of Italy (CNR IGAG), Research Area of Rome 1, 00010 Rome, Italy; aidamaria.conte@cnr.it
* Correspondence: daniela.guglietta@cnr.it

Abstract: The Sidi Bou Othmane (SBO) pegmatite district is situated in the Central Jebilet massif, Western Meseta domain, Morocco. The SBO district is hosted essentially in a volcano-sedimentary series composed of Late-Devonian Sarhlef shales. Pegmatite bodies crop out as dykes, which are oriented from N-S to E-W and are generally variably deformed with ductile and/or brittle structures with ante, syn- or post-kinematic criteria. Petrographic observations of pegmatite dykes show that feldspars (i.e., albite, microcline) are the most abundant mineral phases, followed by quartz and micas, with tourmaline and accessory minerals such as garnet, and zircon also featuring heavily, as well as secondary minerals such as clinochlore, sericite, and illite. The geochemical study of the SBO pegmatites indicates that they have mainly S-type granitic compositions, which are peraluminous granites with calc-alkalic affinities. The study of trace elements indicates that SBO pegmatites were formed in post-orogenic syn-collision context during the Variscan orogeny by the partial melting of argilliferous sediment. They can be ascribed to the muscovite-bearing pegmatite; moreover, they have good potential regarding ceramics. They also contain minerals, such as feldspar, which have been recently assessed as critical raw materials by the European Union.

Keywords: Central Jebilet; Sidi Bou Othmane; pegmatite dykes; syn-collision; s-granite

Citation: Wafik, A.; El Aouad, N.; Daafi, Y.; Morsli, Y.; Chniouar, M.; Punturo, R.; Conte, A.M.; Guglietta, D.; Aba Sidi, W. Geological and Geochemical Characterization of Variscan Pegmatites in the Sidi Bou Othmane District, Central Jebilet Province, Morocco. *Geosciences* **2024**, *14*, 144. https://doi.org/10.3390/geosciences14060144

Academic Editors: Olivier Lacombe and Jesus Martinez-Frias

Received: 20 December 2023
Revised: 20 May 2024
Accepted: 22 May 2024
Published: 24 May 2024

Copyright: © 2024 by the authors. Licensee MDPI, Basel, Switzerland. This article is an open access article distributed under the terms and conditions of the Creative Commons Attribution (CC BY) license (https://creativecommons.org/licenses/by/4.0/).

1. Introduction

Pegmatite has been specified as an igneous rock of mostly granitic composition, featuring properties such as highly coarsened and generally variable crystals, an abundance of strongly directional graphitic or other skeletal crystal growth, and the prominent spatial zonation of mineral assemblages, including monomineralic zones [1–4].

Granitic pegmatites are the main host rocks for rare metal deposits, strategic minerals, and precious/semi-precious gems [5]. They are commonly interpreted as the end products of extreme fractional crystallization of granitic magmas. This fractionation promotes the increase in rare metals and volatiles in the residual melt, leading to mineralization in granitic pegmatites [6,7].

In Morocco, the granitic pegmatites hosted in Precambrian terrains are relatively the most studied [8–17]. The research on Variscan pegmatites, particularly those of the Jebilet Massif, dates back to some decades ago [18–23]. These studies focused on the crystallography of the phosphatic mineral phases and highlighted the presence of frequent monocrystalline ferrisicklerite nodules in the veins of Sidi Bou Othmane (SBO) pegmatites (Jebilet Massif).

Recently, Essaifi et al. [24] pointed out that the shear zones affecting the Tabouchent granodiorite allowed fluid flow on a regional scale, causing the metal zonation observed around the pluton from a proximal Cu-Au mineralization to a Ag-Pb-Zn-Au mineralization.

The Jebilet Massif represents a critical mining district characterized by various ore deposits (e.g., Draa Sfar VMS, Frag al Ma graphite field graphite, SBO district aplo-pegmatite). The SBO pegmatites and Bir Nhass have not been studied so far from a geological point of view despite the research carried out on the Jebilet Massif [25–27]. Detailed petrological and geochemical data, spatial distribution, and the relationships with surrounding rocks and deformation are still unclear.

This study aims to characterize and classify the petrographic and geochemical features of the SBO pegmatites and to identify the associated alteration.

2. Geological Setting

The study area is located at about 30 km to the north of Marrakesh (Morocco). It is geologically situated in the central unit of Jebilet in the Mestian domain (Figure 1) [26,28–30]. The geological framework of the studied region is characterized by a folded Variscan belt primarily consisting of Paleozoic basement formations. These basement rocks have undergone metamorphism, ranging from greenschist to amphibolite facies, and have been intruded by syn- to late-orogenic magmatic intrusions during the Variscan orogeny [31–33]. These formations are exposed below an undeformed cover of Mesozoic to Cenozoic strata.

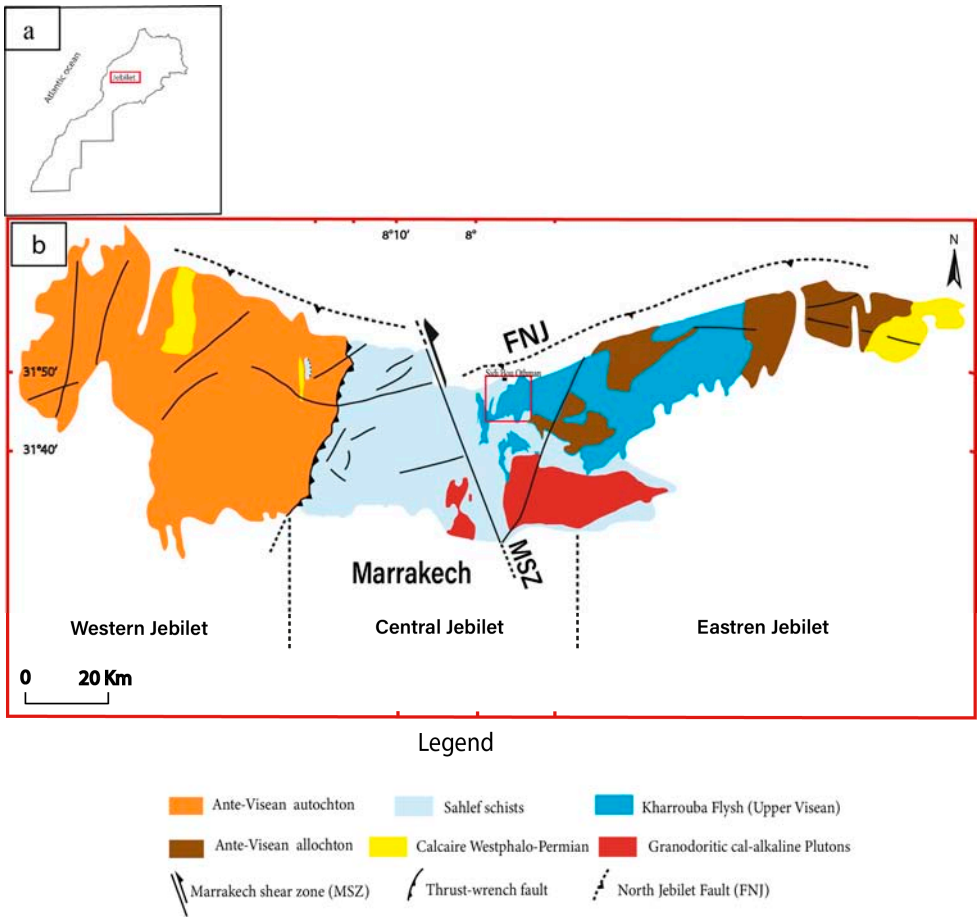
a
Atlantic ocean
Jebilet
b
8°10'
8°
N
FNJ
31°50'
31°40'
Marrakech
MSZ
Western Jebilet
Central Jebilet
Eastren Jebilet
0
20 Km
Legend
Ante-Visean autochton
Sahlef schists
Kharrouba Flysh (Upper Visean)
Ante-Visean allochton
Calcaire Westphalo-Permian
Granodoritic cal-alkaline Plutons
Marrakech shear zone (MSZ)
Thrust-wrench fault
North Jebilet Fault (FNJ)

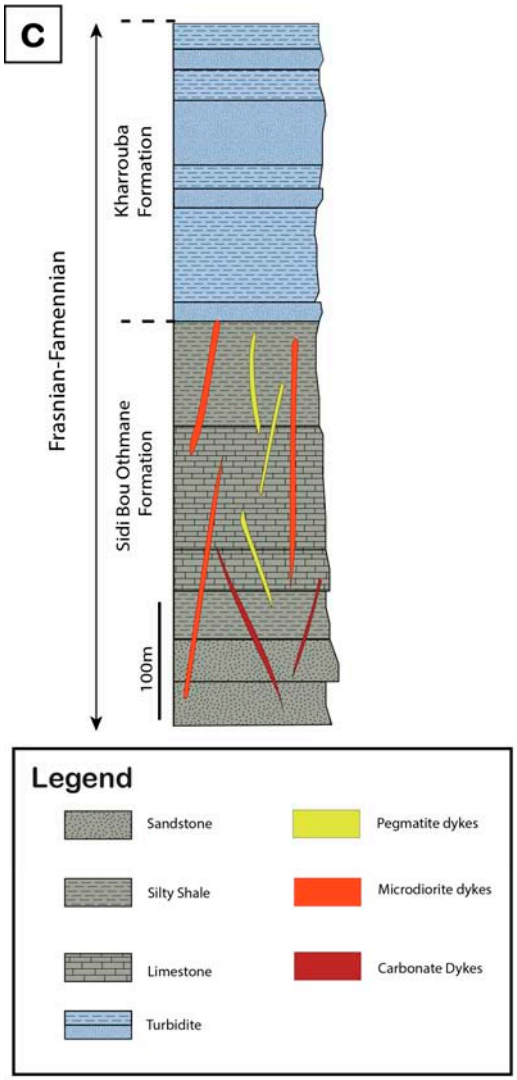

Figure 1. (**a**) Localization of the Jebilet Massif in the Variscan of Morocco; (**b**) geological context of the Variscan Jebilet Massif, showing the location of the SBO study area (modified from Huvelin) [28]; (**c**) synthetic lithostratigraphic column of the SBO area in the Jebilet Massif modified after Bordonaro [30], Delchini [26], Lazreq et al. [29].

The SBO area presents three main geological formations [29,34]:

- A lower formation named the SBO formation, mainly consisting of sandstones, silty shale, and limestone;
- A middle formation named the Kharrouba formation; formed essentially by turbidites, these two series are cut by numerous dykes (pegmatites, microdiorite, carbonates) and were formed during the Frasnian−Famennian extinction;
- An upper formation (Visean) called the Teksim formation, which corresponds to a transgressive series deposited in a platform environment composed of shales, limestones, sandstones, and siltstones.

The field investigations show that 180 E-W dykes are secant on NS pegmatite dykes. Their thicknesses vary from a few centimeters to a few meters (30 cm to 8 m) and they have an extension of a few meters to a few hundred meters (1 m to 500 m). Successively, they underwent a deformation presented on the ground by boudinage, and strike-slip faults shifted their architectures.

Chopin et al. [35] propose two discernible magmatic pulses during the early Carboniferous and late Carboniferous to early Permian periods across the entire Meseta domain, refuting the previous notion of three distinct pulses. The U-Pb method gave ages of 350–

330 Ma to the initial magmatic activity, coinciding with the Eovariscan phase and the formation of intracontinental basins throughout the Meseta. The subsequent magmatic pulse, ranging from 305 to 275 Ma, corresponds with the primary Variscan convergent events within the Meseta amidst a milieu of intracontinental orogeny. This phase is attributed to the collision between Gondwana and the European Variscan belt, marked by the closure of the Paleotethys Ocean propagator tip and succeeded by a direct collision with Laurussia. According to Bouloton et al. 1992 [25,36], the emplacement of these intrusions is accompanied by contact metamorphism in the hornfels facies. On the basis of the mineral assemblage in the metamorphic aureole, pressure conditions were estimated in the range of 2.2 kbar, which corresponds to a maximum depth of 8 km. Differently, the P-T conditions in which the pelitic basement was enclaved and equilibrated during magma ascent have been estimated at about 750 °C and 3.5 kbar (350 MPa) [36].

The Variscan collision event in the Meseta region occurs in two stages during the late Carboniferous to early Permian period. The late Carboniferous event follows the closure of the Rheic Ocean, and the magmatic activity coincides with syn-compressional deformation in neighboring regions, such as Iberia and Central Massif. This late Carboniferous event is followed by an early Permian collision between Gondwana and Laurussia, leading to enhanced late/post-orogenic magmatism in the Meseta region [35–37].

Indeed, the Carboniferous formation underwent a very intense deformation, showing that the Hercynian orogeny stretched out between 330–250 Ma [38]. This deformation results from a succession of tectonic events contemporary to the Hercynian and post-Hercynian orogeny.

Bordonaro [30] outlined five stages of deformation in the Central Jebilet, namely D0 through D4. D0 involved ante-schist deformation marked by large-scale E-W folds linked to syn-sedimentary strike-slip sheets. D1 exhibited syn-schistosity folding with an average N30 direction, transitioning to rectified axial planes from east to west, indicative of regional syn-metamorphism. D2 marked the peak of deformation and metamorphism featuring the folding and shearing of D1 structures. D3 showcased an N110 to N150 crenulation schistosity, featuring a slightly dipping axial plane towards the NE and localized thrusting towards the west. D4 manifested as two sets of conjugate N70 dextral and N135 sinistral strike-slip faults alongside observable zig-zag folds.

Therefore, Delchini et al. [26] reveal two distinct deformation phases shaping the Jebilet Massif from Late Carboniferous to Early Permian. Initially, superficial nappe emplacement, termed D1, induces NS shortening in the Central and Western Jebilet, with ambiguous kinematics being seen in the Eastern Jebilet. Subsequently, D2 involves continuous westward thrusting onto the Coastal Block via the WMSZ, causing significant NW-SE transpressional crustal shortening accompanied by HT-LP metamorphism. The absence of crustal stacking suggests a link between high-temperature metamorphism and post-rift thermal anomalies. As far as P/T metamorphic conditions, according to [26], temperature values vary between 474 ± 50 °C and 628 ± 50 °C, respectively. Moreover, an Early Triassic (ca. 240 ± 10 Ma) magmatic event in the Central Jebilet was responsible for emplacement of a quartz-monzodiorite dyke swarm [39].

These areas underwent a sub-meridian syn-schist folding phase, associated with epizonal metamorphism of the post-upper Visean age, followed by sub-parallel shearing at S1 [40,41]. However, there is also the existence of a peri-plutonic metamorphism that developed around granite intrusions. The brittle tectonics are marked mainly by the existence of directional faults generally from N70° to N90°, creating a sinistral strike-slip fault [42].

3. Materials and Methods

The field investigation did not produce a detailed geological mapping of the pegmatite dykes and structural measurements. At this end, the representative samples have been collected and petrographic observations have been carried out at the laboratories of the Faculty of Sciences of Semlalia, UCA, Marrakesh. Forty thin sections of fresh pegmatite

samples have been prepared and used for minero-petrographic and geochemical investigations. Petrographic analyses have been carried out using a Zeiss Axiolab polarizing microscope. The sample database is set out in Table 1, showing the observed minerals and grain size.

Based on petrographic observations, 25 representative samples have been analyzed for major, trace, and rare earth elements, using inductively coupled plasma atomic emission spectrophotometry (ICP-AES). The major elements have been determined using a WD-XRF spectrometer equipped with five diffraction crystals, using fusion glasses made from a mixture of powdered sample and lithium tetraborate ($Li_2B_4O_7$) in the ratio of 1.5. Calibration is based on 30 certified international standards. The trace and rare earth elements have been analyzed by ICP-MS Laser ablation with the following parameters: spot diameter = 90 μm; frequency = 10 Hz; energy density 20 J/cm^2 in a helium ablation medium. The NIST glass reference material SRM 610 is used as the calibration standard. The analytical accuracy for ICP-MS analyses ranged from ±1–8%.

Table 1. Sampling database reporting, for each selected rock specimen, the mineralogical content and the average grain size.

Sample References	Mineralogical Content (Accessory Minerals)	Grain Size
SBO.01	Quartz, Muscovite, Feldspar (apatite, zircon)	<3.5 cm
SBO.02	Quartz, Muscovite, Feldspar (apatite, zircon)	<1.5 cm
SBO.03	Quartz, Muscovite, Feldspar (apatite, zircon)	<1 cm
SBO.04	Quartz, Feldspar, Tourmaline, Muscovite (apatite, zircon)	1–3 cm
SBO.05	Quartz, Feldspar, Muscovite (apatite, zircon)	0.5 cm–3.5 cm
SBO.06	Quartz, Feldspar, Muscovite (apatite, zircon)	1–3 cm
SBO.07	Quartz, Feldspar, Muscovite (apatite, zircon)	<0.5 cm
SBO.08	Quartz, Feldspar, Tourmaline, Muscovite (apatite, zircon)	<4.5 cm
SBO.09	Quartz, Feldspar, Muscovite, Tourmaline (apatite, zircon)	<1.5 cm
SBO.10	Quartz, Muscovite, Feldspar (apatite, zircon)	<2.5 cm
SBO.11	Quartz, Muscovite, Feldspar (apatite, zircon)	0.5–1.5 cm
SBO.12	Quartz, Feldspar, Muscovite (apatite, zircon)	<3 cm
SBO.13	Muscovite, Feldspar, Quartz (apatite, zircon)	<1.5 cm
SBO.14	Quartz, Feldspar, Muscovite, Tourmaline (apatite, zircon)	0.5–3.5 cm
SBO.15	Quartz, Muscovite, Feldspar, Tourmaline (apatite, zircon)	1–5 cm
SBO.16	Quartz, Feldspar, Muscovite, Tourmaline (apatite, zircon)	2–4.5 cm
SBO.17	Quartz, Muscovite, Feldspar, Tourmaline (apatite, zircon)	2–10 cm
SBO.18	Quartz, Feldspar, Muscovite (apatite, zircon)	1–4.5 cm
SBO.19	Quartz, Muscovite (apatite, zircon)	<2.5 cm
SBO.20	Quartz, Feldspar, Muscovite (apatite, zircon)	<3 cm
SBO.21	Quartz, Feldspar, Muscovite (apatite, zircon)	<2.5
SBO.22	Quartz, Feldspar, Muscovite (apatite, zircon)	<3 cm
SBO.23	Quartz, Muscovite, Feldspar (apatite, zircon)	<1.5 cm
SBO.24	Quartz, Feldspar, Muscovite (apatite, zircon)	<0.3 cm
SBO.25	Feldspar, Muscovite, Quartz (apatite, zircon)	<0.9 cm

4. Results

4.1. Pegmatites Description

The SBO region is characterized by the abundance of pegmatite rocks forming veins and dykes around the area. The occurrence of pegmatite rocks suggests a shallow magma body [26,43,44,45]. Other magmatic products are present in the SBO region and are represented by microdiorite dykes posterior to the pegmatite veins and to the regional

schistosity. Their emplacement is related to rifting during the opening of the Atlantic Ocean [26].

The SBO pegmatites crop out as dykes mainly oriented at N30° (N-S to NNE-SSW) with a sub-vertical dip (Figure 2).

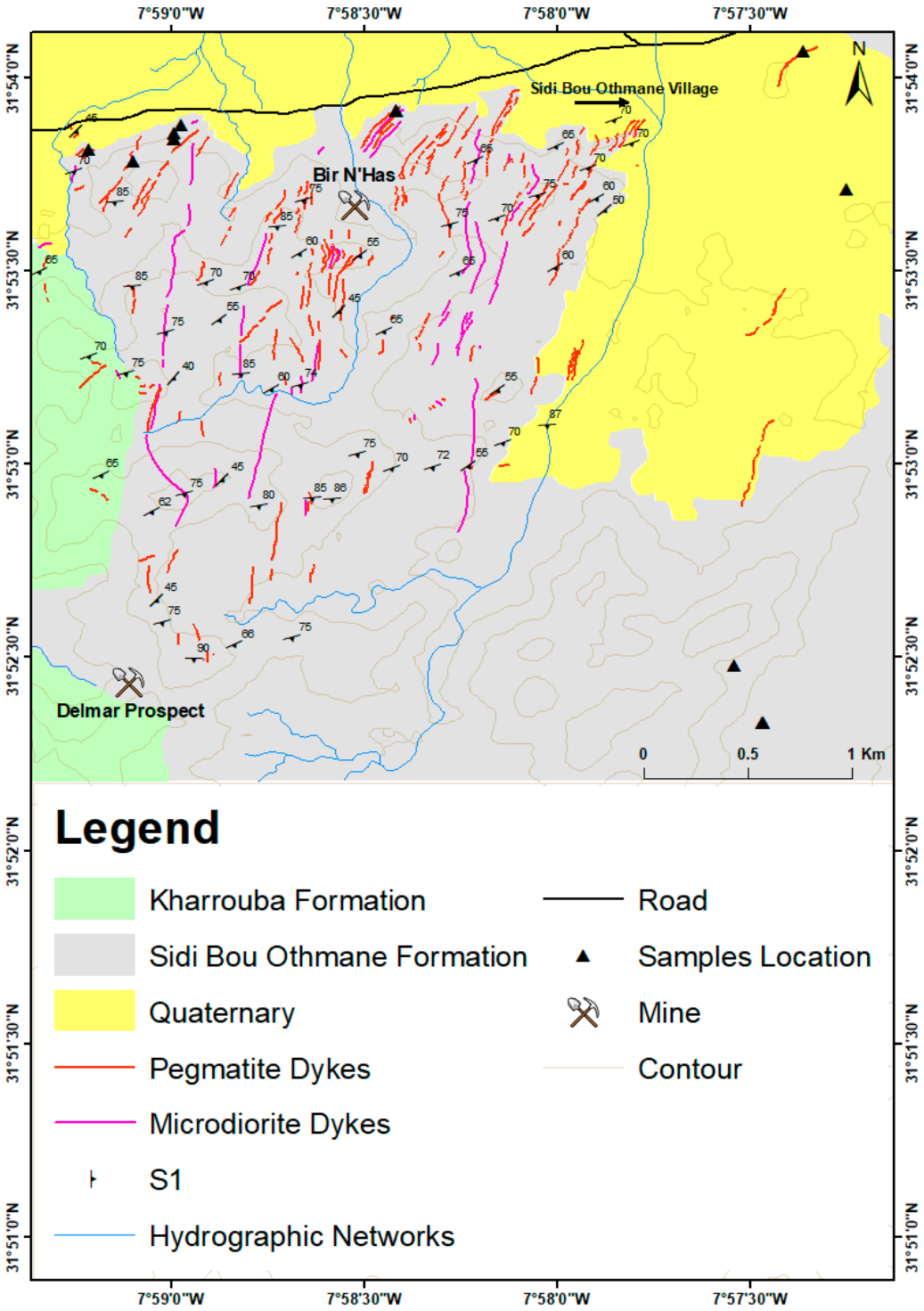

Figure 2. Simplified geological map showing the distribution of the pegmatites within the Sidi Bou Othmane area.

These pegmatites are exclusively hosted in the Sarhlef Shale of the Upper Devonian age (Frasnian–Famennian), covering a large area of the Jebilet central unit [29]. They include an anoxic sedimentation in marine platform environment [45] of sandstone–pelite,

sandstone and pelitic banks (Figure 3a), and at the top, the calcareous sedimentation (Figure 3b). In the study area, the host rock shows alternating levels of metapelite with andalusite and/or cordierite, as well as other unstained sandstone layers free of porphyroblast, ranging from centimeters to meters.

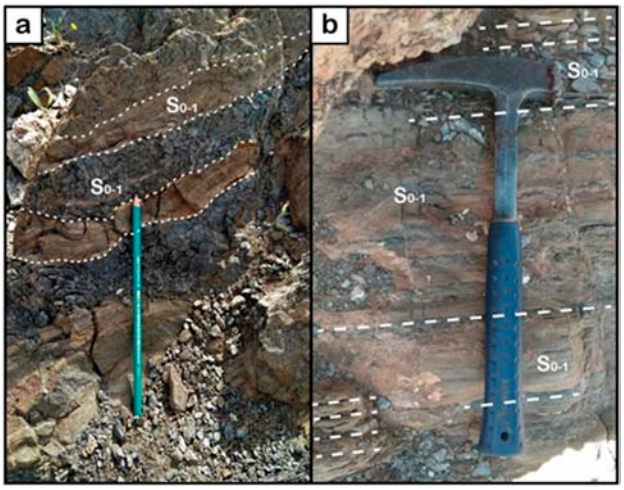

Figure 3. (**a**) The host rock shows alternating between metapelite and sandstone; (**b**) the calcareous levels at the top (S0 is stratification and S1 is schistosity).

Alternatively, SBO pegmatites are mainly constituted by the association of quartz, albite, muscovite, and, sometimes, tourmaline and potassium-rich feldspar (Figure 4).

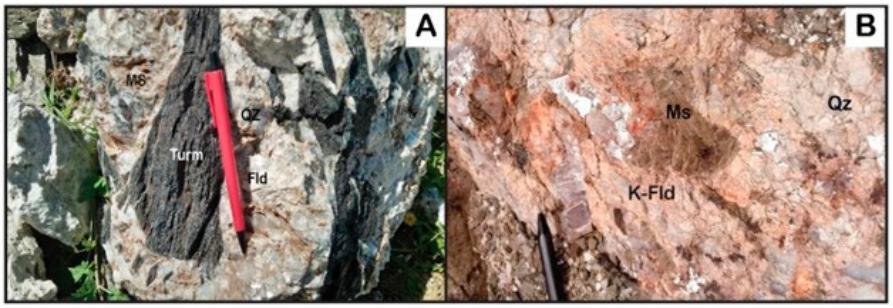

Figure 4. The mineralogy of a pegmatite vein (**A**) with tourmaline (Turm), quartz (QZ) and feldspar (Fld); (**B**) with muscovite (Ms), quartz (QZ) and K-feldspar (K-Fld).

They are generally unzoned but different compared to some zoned pegmatites observed by Agard et al. [20]. Figure 5 shows the zonation, which is quite clear at a large and small scale. A general sequence of internal mineralogical zonation has been extracted from the border to the core (Figure 5):

- The order zone represents a thin layer of a few millimeters in contact with the host rock. Their mineralogy is essentially the same as that of the wall zone;
- The wall zone is formed by quartz and feldspar (mainly albite, muscovite, and tourmaline from a few millimeters to centimeters);
- The intermediate zone is composed of quartz and feldspar. This unit is characterized by a large increase in the crystal size;
- The inner zone (core) is the internal part of the pegmatitic bodies. It is essentially constituted by massive quartz and is mainly a monomineralic part.

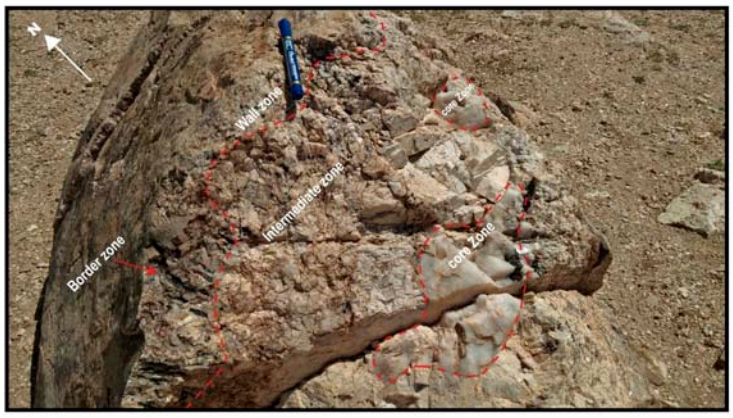

Figure 5. Field picture shows the zonation that has been observed in the pegmatite in SBO area.

4.2. Deformation and Metamorphism

The SBO study area is a part of the Central Jebilet and has undergone an intense tectonic deformation with at least four phases (D1, D2, D3, D4), which resulted in the almost total disappearance of early structures (the stratification S0) [46]. This is the major compressive phase of the Hercynian cycle, showing the Hercynian orogeny stretched out between 330–250 Ma [38]. The deformation allowed for the development of several structures, represented by the S1 schistosity, shear zones, boudins, and folds.

The analysis and study of these structures establish a chronology between the different phases of deformation as well as the possible relationship between these phases.

4.2.1. Schistosity

The S1 schistosity is clearly visible in all the facies by well-developed schistosity in the sandstone metapelites, and it is less tight in the carbonate metapelites. At the scale of the study area, the schistosity trajectories show a direction that varies from N0 to N35, with a dominance of the N20 direction and a dip ranging from 30° to 85° to the west. This schistosity is linked to a strong E-W compression.

Furthermore, in some places it is possible to observe an abrupt variation in the dip of the S1 schistosity towards the east, notably next to the pegmatite dykes. The directions of the S1 schistosity are almost N-S (between N0 and N20). The pole dip rosette shows a concentration of poles on the eastern side, which means that the S1 dips to the west (Figure 6).

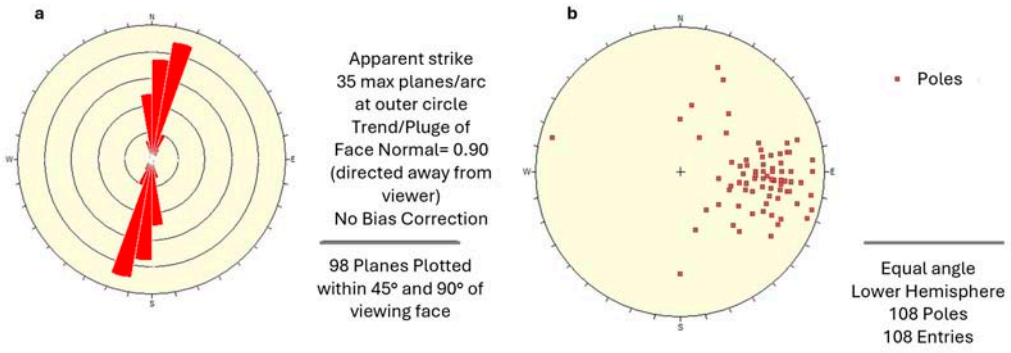

Figure 6. Structural features measured at the scale of (**a**) the outcrop directional rose diagram of the schistosity and (**b**) the pole dip of fold stereoplot.

4.2.2. Folding

The S1 trajectories show that there is, generally a great regularity in the direction and a dip of the planes of S1, with little variable direction from N0° to N30° and a variable dip (in the east, the dip is westward; in the western part of the study area, the dip is eastward).

These results show that the SBO formations have undergone folding (P) that goes with the flow schistosity (S1). The folds, ranging from a few millimeters to a few centimeters, affected the S1. This can be clearly seen in the strike of some pegmatite veins (Figure 7a). During the major deformation, the more competent levels (pegmatites) undergo boudinage (Figure 7b,c) along the planes of the schistosity, forming spindle-shaped crystallization tails at their edges (Figure 7d,e) and showing that the pegmatite setting is syn-deformation. It is also remarkable that the elongation of the small quartz veins intercalated in the schists and parallel to the deformation elongation axis X and perpendicular to the shortening axis Z (Figure 7f).

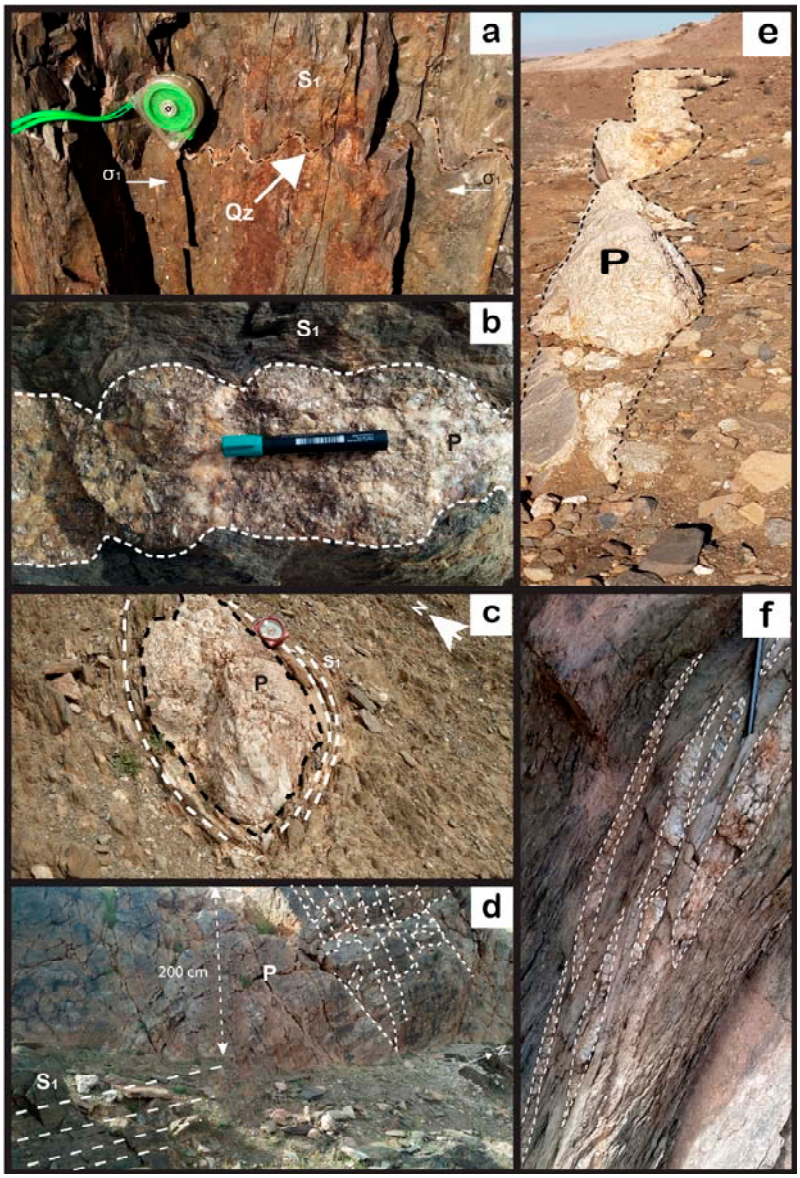

Figure 7. Field pictures showing (**a**) S1 schistosity folding, (**b**,**c**) boudinaged pegmatite dykes, (**d**) diaclases; (**e**) pegmatite boudinaged dike, (**f**) tension jointsin a pegmatite dyke (P: Pegmatite; S1: Schistosity).

Tensile joints are evidence of the shearing that affected the Central Jebilet (Figure 7f). The cracks related to this major phase have an average direction of N10 to N15 and range from cm to dm in size. The filling of these tension joints is generally quartz, in response to the E-W shear.

The brittle tectonic is materialized by a fracturing that affects essentially the pegmatite dykes and the quartz veins, but it can also have an effect at the level of the sandstone bars in the form of diaclases. The microdiorite veins and the quartz-carbonate veins are included in fractures linked to these brittle tectonics.

In the study area, this tectonic is developed at a large extent, materialized essentially by decoupling. It is manifested by a lateral displacement of the magmatic veins (pegmatites, microdiorites), limestone bars, and quartz veins. These early quartz veins and the pegmatite veins are offset by faults of general direction N110 to N140.

4.3. Petrography

The petrographic analysis revealed that quartz, feldspar, plagioclase, muscovite, and tourmaline are common (Table 1) (Figure 8a–f), with some accessory minerals, such as zircon and garnet (Figure 7a), in the SBO rocks. Feldspar is the dominant mineral phase and albite is the most common feldspar. By modal analysis, albite constitutes most of the analyzed samples (>47 vol%) while microcline and anorthite are less than 3%. Albite presents deformation bands in the direction of elongation (Figure 8c–f). It appears in the form of elongated rod-like sections, with sharp cleavages parallel and perpendicular to the elongation of the mineral. This mineral is very altered in illite and sericite (Figure 8c–f).

After feldspar, quartz is the most abundant mineral in SBO pegmatites (Figure 8a–f). It is marked by patches of xenomorphic crystals, and it also occurs as inclusions in feldspar and muscovite. Also, other prominent criteria in quartz are the undulose extinction, chessboard patterns (Figure 8e), and triple points that indicate that the mineral underwent deformation.

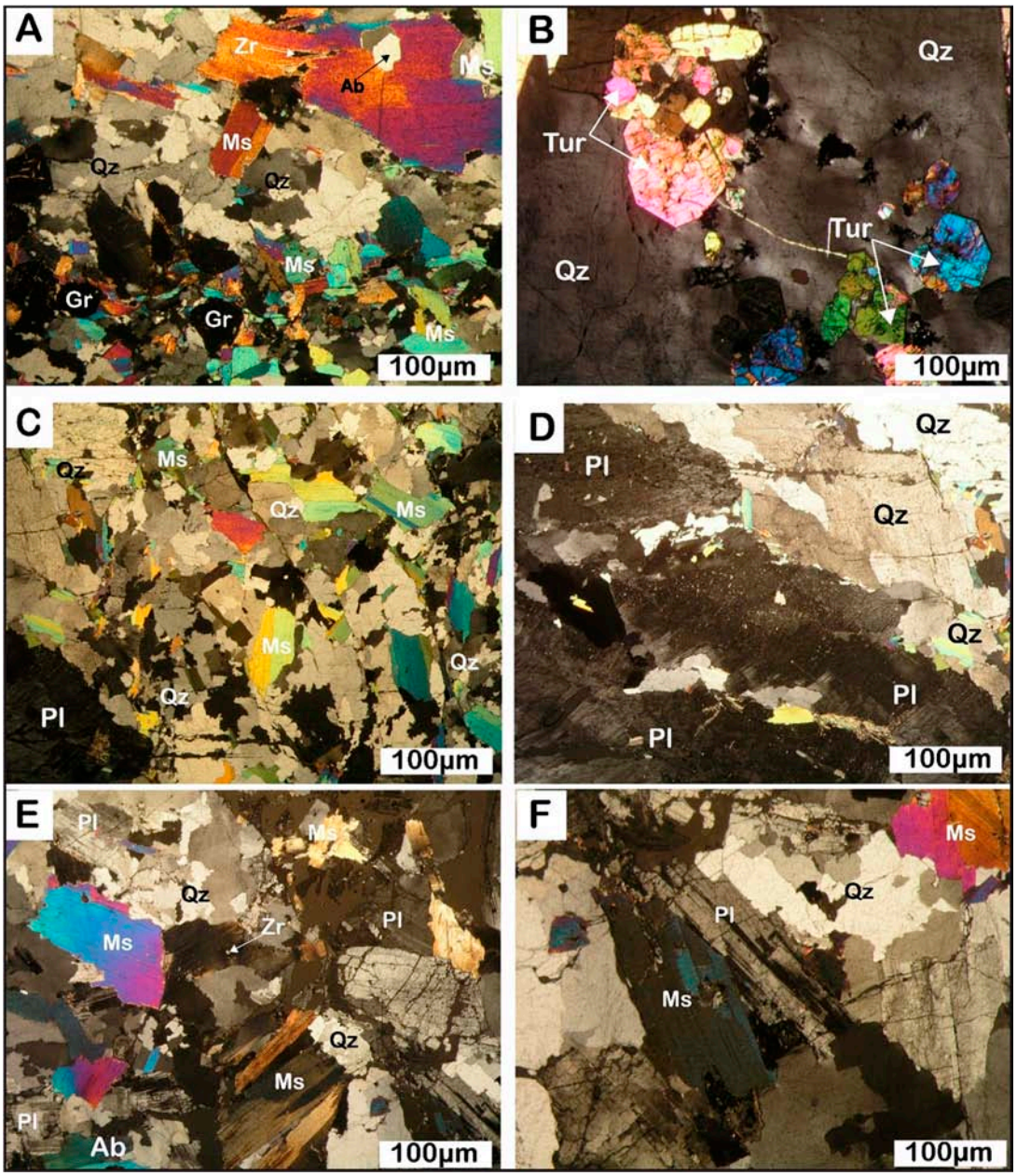

Figure 8. Photomicrographs showing (**a**) large muscovite (Ms), albite (Ab) and quartz (Qz) crystals, garnet (Gr) and zircon (Zr); (**b**) large quartz with tourmaline (Tur); (**c**,**d**) sheared area with plagioclase (Pl), quartz (Qz) and muscovite (Ms); (**e**,**f**) large patches of cataclastic plagioclase (Pl) (albite Ab) with and quartz (Qz), and muscovite (Ms).

Muscovite occurs as euhedral crystals, which are large elongated subautomorphic sheets or micaceous tablets with irregular contours (Figure 8a,e,f). In some cases, muscovite is deformed, showing undulose extinction. This mineral can be observed either as gigantic minerals (cm in size) or as small inclusions within plagioclase. Muscovite sometimes shows a preferential orientation along the schistosity plane. Among micas, biotite occurs with tiny crystals.

Tourmaline is usually found both as basal subhedral and elongated sections, and irregular fractures may occur (Figure 8b).

Among the accessory mineral phases, it is worth noting the occurrence of garnet in some specimens (Figure 8a). Garnet is very rich in muscovite and tourmaline inclusions. Zircon is also present in many specimens (Figure 8a,e).

4.4. Whole Rock Geochemistry

Major, minor, and trace element contents, including rare earth elements (REEs), have been used to highlight the distinct geochemical characteristics of rock types (Tables 2–4) and to make normative calculations (Tables 5–7).

Table 2. Major elements (wt%) of SBO pegmatite dykes. b.d.: Below detection limits.

Sample	SiO_2	Al_2O_3	Fe_2O_3	FeOtot	CaO	MgO	K_2O	MnO	TiO_2	P_2O_5	Na_2O	SO_3
SBO-01	77.04	14.3	0.48	0.432	0.25	b.d.	2.13	0.03	0.01	0.19	4.05	0.61
SBO-02	74.84	14.84	0.37	0.333	<0.10	b.d.	1.97	0.04	0.01	0.62	5.64	0.57
SBO-03	73.05	15.52	0.88	0.792	0.74	0.10	3.9	0.07	0.01	0.58	3.74	0.63
SBO-04	78.94	13.3	1.26	1.134	0.29	0.12	2	0.05	0.02	0.13	2.05	0.63
SBO-05	77.52	14.03	0.74	0.666	0.27	b.d.	3.7	0.03	0.01	0.16	0.90	0.65
SBO-06	72.51	16.11	0.99	0.891	0.72	b.d.	3.77	0.07	0.01	0.60	3.82	0.62
SBO-07	74.06	16.24	<0.10	b.d	0.21	b.d.	1.3	0.02	0.01	0.14	6.63	0.63
SBO-08	74.84	15.72	0.75	0.675	0.53	b.d.	3.55	0.17	0.02	0.36	0.96	0.60
SBO-09	75.41	15.25	0.95	0.855	0.50	b.d.	3.52	0.14	0.02	0.29	0.44	0.60
SBO-10	76.47	14.08	1.02	0.918	0.54	0.1	3.83	0.07	0.04	0.36	0.16	0.62
SBO-11	72.82	15.63	0.34	0.306	0.73	b.d.	3.23	0.10	0.01	0.76	5.10	0.69
SBO-12	73.6	16.51	0.5	0.45	0.29	b.d.	5.27	0.03	0.01	0.23	0.24	0.61
SBO-13	71.09	19.45	<0.10	b.d	0.33	b.d.	4.96	0.02	0.01	0.15	0.33	0.68
SBO-14	73.57	17.46	0.23	0.207	0.18	b.d.	4.50	0.02	0.01	0.12	0.55	0.70
SBO-15	77.07	13.94	0.22	0.198	0.3	b.d.	0.71	0.03	0.01	0.38	5.76	0.62
SBO-16	74.97	14.08	0.6	0.54	1.27	b.d.	1.93	0.14	0.01	0.89	4.23	0.62
SBO-17	69.91	18.71	0.97	0.873	1.14	0.16	3.97	0.03	0.07	0.8	0.42	0.63
SBO-18	72.04	17.45	0.39	0.351	0.70	b.d.	2.52	0.07	0.02	0.59	3.73	0.60
SBO-19	72.6	17.93	0.7	0.63	0.37	b.d	4.00	0.04	0.02	0.23	0.72	0.64
SBO-20	74.79	14.68	0.82	0.738	0.62	b.d	2.04	0.22	0.01	0.88	4.26	0.66
SBO-21	80.21	12.04	0.64	0.576	0.49	v	0.42	0.18	0.01	0.21	4.94	0.61
SBO-22	74.83	14.66	4.21	3.789	0.46	0.10	0.35	0.09	0.03	0.25	3.84	0.71
SBO-23	69.47	18.29	1.39	1.251	1.11	0.63	3.12	0.08	0.22	0.41	0.36	0.51
SBO-24	74.47	16.06	2.35	2.115	0.43	0.23	0.81	0.05	0.03	0.20	4.41	0.65
SBO-25	74.05	15.9	1.62	1.458	0.56	b.d	1.78	0.05	0.01	0.24	4.02	0.61
SBO-26	76.01	15.59	1.16	1.044	0.31	b.d	1.38	0.04	0.01	0.21	4.11	0.63

Table 3. Minor, minor trace, and rare earth elements of SBO pegmatite dykes. Contents are expressed as ppm., n.d. = not detected.

Sample	Ti	K	As	P	Ba	Be	Bi	Cd	Co	Cr	Cu	Li	Mo	Nb	Ni	Pb	Rb	Sb	Sc	Se	Sn
SBO-01	59.951	45	172	829.16	29.3	6.3	15.8	4.8	n.d.	108.3	9.3	143	6.1	14.6	6.7	n.d.	333.3	31.3	7	n.d.	22.7
SBO-02	59.951	42	87	2705.68	22.7	10.4	14.1	1.9	n.d.	35	5.6	98.7	n.d.	37.8	n.d.	n.d.	359.9	2.2	5.7	n.d.	44.3
SBO-03	59.951	83	93	2531.12	101.8	5.4	12.2	2.3	n.d.	116	6.4	141.7	1.9	44.1	1.1	n.d.	759.5	10.5	5.9	n.d.	28
SBO-04	119.902	42	77	567.32	17.1	4.3	4.5	0.9	n.d.	57.9	7	130.6	n.d.	n.d.	11.5	n.d.	338.5	n.d.	6.2	n.d.	27
SBO-05	59.951	79	74	698.24	35.5	6.4	20	1.9	n.d.	176.6	8	208.9	1.3	46.7	<0.1	n.d.	1201	n.d.	5.2	n.d.	107.4
SBO-06	59.951	80	101	2618.4	92.1	5.2	18.5	2.8	n.d.	111.3	4.7	128.4	n.d.	43.7	n.d.	n.d.	716.6	n.d.	5.6	2.9	27.9
SBO-07	59.951	28	87	610.96	24.8	5.5	15.4	1.2	47.3	90.4	9.3	193.4	4.5	3.7	9.5	n.d.	446	5	4.6	4.4	31.4
SBO-08	119.902	75	57	1571.04	58.7	4.6	22.2	1.5	n.d.	39.2	3.5	170.5	3.8	n.d.	2.4	n.d.	408.7	1.4	6.6	n.d.	27.1
SBO-09	119.902	75	46	1265.56	34.7	3.9	n.d.	1.7	n.d.	174.2	5.1	155.1	n.d.	12.1	10.8	n.d.	435.9	9.7	7.1	n.d.	24.3
SBO-10	239.804	81	62	1571.04	51.1	3.6	n.d.	2.6	n.d.	48.2	5.7	191.6	n.d.	9.8	<0.1	n.d.	471.1	14.2	7.5	n.d.	41.5
SBO-11	59.951	69	205	3316.64	13.4	6.8	n.d.	5	n.d.	38.5	6.9	140.4	7.1	20.8	9.8	n.d.	847.4	n.d.	5.6	n.d.	14.2
SBO-12	59.951	112	72	1003.72	151.9	7.8	20.6	1.6	n.d.	37	4.3		2.8	44.2	3.7	n.d.	868.2	10.5	5.2	n.d.	50.4

SBO-13	59.951	105	209	654.6	33.2	8	18.5	5.9	200.3	83.7	8.7	153.7	7.2	49.6	19	n.d.	1571	<0.1	4	<0.1	102.6
SBO-14	59.951	96	201	523.68	46.7	4.9	13.8	5.2	17.2	158.6	8.3	39.4	n.d.	74.6	16.9	n.d.	1466	n.d.	4	0.9	71.2
SBO-15	59.951	15	109	1658.32	22.7	3.3	21.5	2.1	n.d.	164.2	8	19.3	10.7	190	10.2	16.7	272.8	16.7	4.8	n.d.	19.8
SBO-16	59.951	41	115	3883.96	26.9	8.6	0.9	2.9	n.d.	34.3	7.6	247.9	2.6	36.1	9.3	n.d.	700	5	6.2	5	51.4
SBO-17	419.657	84	46	3491.2	154.3	3.9	n.d.	0.6	n.d.	50.1	6.4	119.3	1.3	33.4	20.9	n.d.	585.8	1.9	4.8	3.9	62.9
SBO-18	119.902	54	65	2574.76	46.9	7.9	9.5	1	n.d.	132.8	3.4	38.8	1.2	8.5	25.5	n.d.	385.2	n.d.	3.6	n.d.	26.5
SBO-19	119.902	85	66	1003.72	83.9	9.4	n.d.	2.5	n.d.	50	4.2	71.2	n.d.	35.2	0.2	n.d.	842.5	21.1	5.2	n.d.	41.6
SBO-20	59.951	43	42	3840.32	16.5	4.5	13.5	3.9	n.d.	38.7	4.1	141.7	n.d.	21.7	1.1	7.7	716.6	12.1	5.9	n.d.	22.4
SBO-21	59.951	9	112	916.44	10	3.8	n.d.	2.5	n.d.	145.1	3.3	16.9	n.d.	n.d.	16.4	n.d.	28.6	15.1	6.6	21.4	0.6
SBO-22	179.853	7	345	1091	20.8	3.6	18.3	8.9	n.d.	231.1	11.5	44.3	13.7	n.d.	11.8	n.d.	72.4	n.d.	5.9	n.d.	6
SBO-23	1.318.922	66	138	1789.24	551.5	10	n.d.	2.7	n.d.	59.3	8.2	1893	1.1	48	12.2	n.d.	1714	3	9.6	14.5	415.7
SBO-24	179.853	17	122	872.8	18.6	3.3	21	2.9	n.d.	206.8	23.6	36.3	0.7	<0.1	18.7	n.d.	84.99	n.d.	6.1	n.d.	2.5
SBO-25	59.951	38	121	1047.36	12.7	3.7	11	2.9	45.8	51.9	7.6	74.7	5.4	7.3	19.7	n.d.	248.4	16.7	7.1	n.d.	16.8
SBO-26	59.951	29	32	916.44	9.1	4.5	16.4	0.5	n.d.	145.8	5.6	176.6	4.9	1	<0.1	n.d.		9.4	5.2	n.d.	20.3

Table 4. Minor, minor trace and rare earth elements of SBO pegmatite dykes. Contents are expressed as ppm., n.d. = not detected. (continued).

Sample	**Sn**	**Sr**	**Th**	**U**	**V**	**Y**	**Zn**	**Zr**	**La**	**Ce**	**Pr**	**Nd**	**Sm**	**Eu**	**Gd**	**Tb**	**Dy**	**Ho**	**Er**	**Tm**	**Yb**	**Lu**	**PF**	**Cl**
SBO-01	22.7	51.4	0.5	1.1	2.1	0.6	49.6	9.1	1	1.3	0.3	0.8	0.6	0.1	0.4	0	0.2	0.1	0.1	0.1	0.1	0.1	0.96	465.3
SBO-02	44.3	85.3	1.3	4	3	0.8	39.4	17.7	1.2	1.9	0.3	0.9	0.7	0	0.5	0	0.3	0.1	0.1	0.1	0.1	0.1	1.01	310.2
SBO-03	28	135.7	1.3	1.5	3	2	69.2	13.7	1.1	1.8	0.4	1.6	0.9	0.3	0.8	0.1	0.5	0.1	0.2	0.1	0.2	0.1	0.93	443.1
SBO-04	27	39.8	0.7	0.5	5.7	0.8	36.8	9.4	1	1.5	0.3	0.8	0.6	0	0.5	0	0.2	0.1	0.2	0.1	0.1	0.1	1.08	819.8
SBO-05	107.4	90.8	0.8	1.2	1.3	0.9	38.3	11.4	1.2	1.2	0.3	0.9	0.7	0.1	0.6	0.1	0.5	0.1	0.2	0.1	0.1	0.1	1.49	886.3
SBO-06	27.9	126.5	1.3	1.6	2.5	1.9	62	12.7	1.1	2.1	0.4	1.6	0.9	0.3	0.8	0.1	0.7	0.1	0.2	0.1	0.2	0.1	0.82	576.1
SBO-07	31.4	50.7	0.5	0.1	1.7	0.5	19.1	6.2	0.8	0.9	0.2	0.7	0.6	0.1	0.4	0	0.2	0.1	0.1	0.1	0.1	0.1	0.72	310.2
SBO-08	27.1	50.4	1.8	5.1	4.2	5	32.9	17	1.7	3.5	0.6	1.8	1	0.2	0.9	0.2	1	0.2	0.5	0.2	0.7	0.1	1.64	731.2
SBO-09	24.3	44	0.8	1.6	4.1	1.9	39.1	11.9	1.1	2.1	0.4	1.1	0.7	0.2	0.6	0.1	0.5	0.1	0.3	0.1	0.3	0.1	1.94	775.5
SBO-10	41.5	44.7	1.4	3.5	3.9	3.5	49.3	17.9	1.6	3.1	0.5	1.6	0.9	0.1	0.8	0.1	0.7	0.2	0.4	0.2	0.6	0.1	1.76	753.3
SBO-11	14.2	131	0.7	1.6	3.2	0.8	59.2	15.8	0.9	1.1	0.3	0.7	0.6	0.1	0.5	0	0.2	0.1	0.1	0.1	0.1	0.1	0.67	421
SBO-12	50.4	53.4	0.8	1.5	2.8	0.9	30.4	17.7	1	1.4	0.3	0.8	0.6	0.2	0.5	0	0.3	0.1	0.2	0.1	0.1	0.1	2.36	531.8
SBO-13	102.6	48.6	0.5	1.3	5.1	0.7	59.5	66.8	0.9	1	0.2	0.7	0.6	0.1	0.4	0	0.2	0.1	0.1	0.1	0.1	0.1	2.47	265.9
SBO-14	71.2	66.8	0.6	1.7	3.2	0.7	14.8	37.5	0.7	0.6	0.2	0.6	0.6	0.1	0.4	0	0.2	0.1	0.1	0.1	0.1	0.1	2.31	332.3
SBO-15	19.8	80.3	3.3	1.6	0.8	2.6	22	13.7	1.4	3.1	0.5	2.1	1.1	0.2	1	0.1	0.7	0.1	0.3	0.1	0.2	0.1	0.66	841.9
SBO-16	51.4	86.2	1.1	2.5	2.8	3.9	109.6	15.4	2.3	3.7	0.6	2.6	1.4	0.9	1.5	0.2	0.8	0.1	0.3	0.1	0.2	0.1	1.54	398.8
SBO-17	62.9	75.9	1.2	1.3	14.1	2.6	25.7	10.6	2.9	5.8	0.8	3	1.1	0.7	0.9	0.1	0.6	0.2	0.4	0.1	0.3	0.1	2.34	797.6
SBO-18	26.5	94.7	3.6	3.3	5.4	5.9	24.4	13.6	2.2	3.8	0.6	2.3	1.5	0.3	1.6	0.3	1.6	0.2	0.4	0.1	0.3	0.1	1.74	841.9
SBO-19	41.6	52.7	1.7	0.8	3.9	1.3	25.7	8.7	1.2	1.5	0.3	1	0.7	0.2	0.6	0.1	0.4	0.1	0.2	0.1	0.1	0.1	2.07	598.2
SBO-20	22.4	116.8	1.1	10.9	2.2	1.2	206.8	25	0.9	1.1	0.3	0.8	0.6	0	0.5	0	0.3	0.1	0.2	0.1	0.2	0.1	0.9	288
SBO-21	0.6	38.1	1.3	9.2	<0.1	5.6	14	20.3	2	4.1	0.6	1.9	1	0	0.9	0.1	1	0.3	0.6	0.2	1.1	0.2	0.22	310.2
SBO-22	6	69.3	1.5	2.7	5.8	2.5	117.4	17.5	1.5	2.3	0.4	1.3	0.9	0.1	0.7	0.1	0.6	0.1	0.3	0.1	0.4	0.1	0.39	332.3
SBO-23	415.7	164.3	5.5	1.3	63.9	8.7	107.2	33.1	15.2	29	3.4	12.5	2.6	1.2	2.5	0.3	1.8	0.4	1	0.2	0.9	0.2	3.57	398.8
SBO-24	2.5	40.5	0.8	1.2	3.2	1.7	66.9	18.2	1.6	3	0.5	1.5	0.8	0.1	0.6	0.1	0.3	0.1	0.2	0.1	0.3	0.1	0.4	310.2
SBO-25	16.8	50.7	3.7	2.2	6.3	1.3	52.9	15.9	1.5	5.3	0.5	1.6	1	0.1	0.7	0.1	0.4	0.1	0.2	0.1	0.4	0.1	1.12	709
SBO-26	20.3	48.1	1.1	0.5	1.4	0.8	41.5	7.7	0.8	1.3	0.2	0.7	0.6	0	0.5	0	0.2	0.1	0.1	0.1	0.1	0.1	0.76	753.3

Table 5. CIPW norm Holacher calculation for Sidi Bou Othmane pegmatites.

Minerals Weight %	SBO-01	SBO-02	SBO-03	SBO-04	SBO-05	SBO-06	SBO-07	SBO-08	SBO-09	SBO-10	SBO-11	SBO-12	SBO-13	SBO-14
Quartz	52.09	54.38	33.77	52.42	45.22	45.69	53.23	51.78	36.45	38.84	36.36	33.24	44.69	47.60
Plagioclase	0.00	0.20	38.63	28.52	32.24	35.36	0.00	38.86	43.99	27.52	31.30	52.13	31.72	33.06
Orthoclase	29.31	29.31	19.09	2.07	11.41	12.59	31.14	2.48	11.64	23.05	18.44	7.68	12.06	4.79
Corundum	14.08	12.03	4.62	8.62	5.63	4.24	10.81	3.85	4.16	5.95	8.31	4.67	6.27	8.76
Hypersthene	0.02	0.20	0.28	3.60	0.73	0.41	0.44	0.84	1.35	0.80	0.92	0.11	1.07	2.30
Ilmenite	0.02	0.02	0.02	0.06	0.02	0.02	0.02	0.02	0.02	0.02	0.42	0.04	0.02	0.06
Magnetite	0.00	0.33	0.49	6.10	0.87	0.70	0.72	0.93	0.54	1.15	2.02	0.00	1.19	3.41
Apatite	0.35	0.28	1.76	0.58	2.06	0.44	0.53	0.49	1.44	1.34	0.95	0.32	2.04	0.46
Zircon	0.01	0.01	0.00	0.00	0.00	0.00	0.00	0.00	0.00	0.00	0.00	0.00	0.00	0.00
Chromite	0.00	0.03	0.01	0.04	0.01	0.03	0.01	0.03	0.01	0.03	0.01	0.01	0.01	0.01
Anhydrite	1.16	0.00	0.00	0.00	0.00	0.00	0.00	0.00	0.00	0.00	0.00	0.00	0.00	0.00
Na_2SO_4	0.00	1.24	1.22	1.26	1.10	1.08	1.08	1.08	1.01	1.12	0.90	1.12	1.17	1.15
Total	97.04	98.03	99.89	103.27	99.29	100.56	97.98	100.36	100.61	99.82	99.63	99.32	100.24	101.60
Fe3+/(Total Fe) in rock	0.0	49.6	49.7	50.0	50.0	50.1	50.0	49.8	36.5	49.0	50.0	0.0	49.9	49.9
Ca/(Ca + Na) in rock	100.0	15.3	7.3	6.2	14.2	14.8	40.0	5.2	0.0	0.0	14.1	1.7	7.4	0.6
Ca/(Ca + Na) in plagioclase	0.0	65.2	0.0	2.2	1.5	13.7	0.0	2.6	0.0	0.0	9.1	0.3	0.0	0.0
Differentiation Index	81.4	83.9	91.5	83.0	88.9	93.6	84.4	93.1	92.1	89.4	86.1	93.1	88.5	85.5
Calculated density. g/cc	2.76	2.74	2.68	2.84	2.71	2.69	2.74	2.69	2.69	2.70	2.75	2.67	2.72	2.79
Calculated liquid density	2.37	2.36	2.36	2.44	2.37	2.36	2.36	2.35	2.36	2.37	2.41	2.36	2.37	2.40
Calculated viscosity. dry	12.4	12.8	10.2	9.9	11.7	12.2	12.8	13.8	11.0	10.8	9.1	10.8	11.5	10.6
Calculated viscosity. wet	9.0	8.9	7.3	7.3	7.9	8.3	8.9	8.6	7.7	7.7	7.1	7.7	7.9	7.7
Estimated liquidus temp.	783	755	791	802	746	726	750	665	755	779	853	763	755	784
Estimated H_2O content	4.13	4.45	4.04	3.91	4.53	4.76	4.49	5.43	4.42	4.17	3.32	4.34	4.43	4.10

Table 6. CIPW norm Holacher calculation for Sidi Bou Othmane pegmatites. (continued).

Minerals Weight %	SBO-15	SBO-16	SBO-17	SBO-18	SBO-19	SBO-20	SBO-21	SBO-22	SBO-23	SBO-24	SBO-25	SBO-26	SBO-28	SBO-27
Quartz	45.70	47.59	61.27	60.62	61.25	43.55	57.83	61.10	53.90	43.22	38.04	42.07	20.95	97.68
Plagioclase	30.61	30.84	13.81	3.68	0.00	44.68	4.52	0.95	0.36	0.00	27.75	28.26	39.54	0.00
Orthoclase	10.52	10.52	11.82	21.87	22.63	4.20	20.98	20.80	23.46	9.35	23.64	16.37	24.29	0.00
Corundum	7.92	7.63	8.35	9.25	9.93	4.49	10.94	11.26	14.34	0.00	8.14	7.62	0.08	0.00
Hypersthene	1.41	0.99	1.47	0.63	1.15	0.21	0.89	0.42	1.13	0.00	0.61	0.91	9.23	0.00
Ilmenite	0.02	0.02	0.04	0.02	0.08	0.02	0.04	0.04	0.13	0.57	0.04	0.02	1.46	0.02
Magnetite	2.35	1.68	1.83	1.07	1.48	0.32	1.09	1.23	1.41	0.00	1.01	1.44	8.02	0.00
Apatite	0.56	0.49	0.30	0.37	0.83	0.88	0.83	0.67	1.85	0.00	0.53	1.39	0.44	0.09
Zircon	0.00	0.00	0.00	0.00	0.00	0.00	0.00	0.00	0.00	0.00	0.00	0.00	0.01	0.00
Chromite	0.01	0.03	0.01	0.04	0.01	0.03	0.01	0.04	0.01	0.00	0.01	0.03	0.01	0.00
Anhydrite	0.00	0.00	0.00	0.00	0.18	0.00	0.00	0.30	0.24	1.06	0.00	0.00	0.00	0.00
Na_2SO_4	1.08	1.12	1.12	1.15	0.91	1.10	1.06	0.75	0.87	0.00	1.14	1.10	0.28	0.00

Total	100.18	100.91	100.02	98.70	98.45	99.48	98.19	97.56	97.70	98.56	100.91	99.21	104.31	98.16
Fe3+/(Total Fe) in rock	50.0	50.1	45.8	49.8	49.9	49.7	50.2	60.5	50.1	50.1	50.0	50.0	50.0	0.0
Mg/(Mg + Total Fe) in rock	0.0	0.0	0.0	0.0	8.8	0.0	0.0	0.0	14.1	0.0	0.0	0.0	29.4	0.0
Mg/(Mg + Fe2+) in rock	0.0	0.0	0.0	0.0	16.2	0.0	0.0	0.0	24.7	0.0	0.0	0.0	45.5	0.0
Mg/(Mg + Fe2+) in silicates	0.0	0.0	0.0	0.0	26.6	0.0	0.0	0.0	41.8	0.0	0.0	0.0	69.0	0.0
Ca/(Ca + Na) in rock	5.6	4.0	7.3	14.2	65.1	2.8	23.4	38.6	60.0	9.4	5.2	9.4	44.7	100.0
Ca/(Ca + Na) in plagioclase	1.8	0.6	4.0	8.3	0.0	0.0	6.8	0.0	0.0	0.0	1.3	0.0	44.7	0.0
Differentiation IndexI would avoid this part. otherwise, we explain the software in a detailed manner	86.8	89.0	86.9	86.2	83.9	92.4	83.3	82.9	77.7	85.7	89.4	86.7	84.8	97.7
Calculated density. g/cc	2.75	2.73	2.75	2.74	2.76	2.68	2.76	2.76	2.80	2.73	2.72	2.73	2.82	2.65
Calculated liquid density	2.39	2.37	2.36	2.35	2.37	2.35	2.37	2.36	2.40	2.37	2.38	2.38	2.53	2.23
Calculated viscosity. dry	11.0	11.7	14.2	14.5	14.2	12.6	13.3	14.1	11.0	11.0	10.1	10.6	5.2	25.6
Calculated viscosity. wet	7.8	8.1	9.1	9.3	9.2	8.3	9.0	9.3	8.2	8.0	7.5	7.7	4.6	5.9
Estimated liquidus temp.	775	749	683	691	703	707	733	713	819		811	789	1002	303
Estimated H_2O content	4.20	4.49	5.23	5.16	5.02	4.97	4.68	4.90	3.71		3.79	4.04	1.76	7.65

Table 7. CIPW norm calculation for SBO pegmatites from maximum to minimum Na_2O contents.

	SBO-PG7	**SBO-PG12**
Q	30.5	67.0
A	7.7	7.7
P	56.2	2
F	0.0	0.0
Total	100	100

The geochemical data of the SBO pegmatites samples show a wide range of major elements with silica (SiO_2) contents ranging from 69.47 to 80.21 wt%. Al_2O_3 contents are generally high, ranging from 12.04 to 19.45 wt%; on the other hand, the other oxides are lower at $Na_2O \leq 5.76$; $K_2O \leq 5.27$ wt%; $Fe_2O_3 \leq 5.53$, $FeO \leq 4.98$ wt%; $MgO \leq 2.33$ and $TiO_2 \leq 0.77$ wt%, $CaO \leq 3.86$%, $MnO \leq 0.22$ wt%, $P_2O_5 \leq 0.89$ wt%. The Loss On Ignition (L.O.I.) shows values between 0.22 and 3.57 wt%. As far as the minor and trace elements analyzed from the pegmatite, Sr ranges between 38 and 164 ppm. The compatible elements show low to high concentrations, ranging from 0 to 25.50 ppm for Ni and from 25 to 231 ppm for Cr. In most samples, the low concentrations of these compatible elements suggest that the materials that formed the pegmatite are probably derived from a depleted source [47].

Zr values range from 6 to 66 ppm and are related to the accessory zircon, which is the main mineral phase in which this element is concentrated. Ba concentration varies

from 9 to 551 ppm. The Ba is mainly detected in biotite and has a high affinity for potassium feldspar, in substitution to K [48]. Rb contents are relatively high, up to 1714 ppm; this element is generally incorporated in minerals such as biotite and potassium feldspar.

Furthermore, Ta and Nb contents range, respectively, from 0.8 to 4.2 ppm and 0 and 190 ppm. Li and Cs values comprise between 2.3 and 1893 ppm and 0.2 to 277 ppm, respectively. Sn values reach 415 ppm. The concentrations of Nb, Ta, Sn, and Cs are relatively high and indicate enrichment within these rocks. Li reaches the highest concentrations among trace elements. This can be explained by highly enriched sources.

The sum of the REEs concentrations of the SBO pegmatites range from 3.9 to 70 ppm, which is lower compared to the international range (250–270 ppm) of Cuney et al., 1987[49]. The depletion of REEs has been attributed to various processes, including magmatic differentiation [50], hydrothermal leaching [51], and or a combination of both. The sum of light rare earth element (ΣLREE) and the sum of heavy rare earth element (ΣHREE) concentration values for the pegmatite samples vary within the range of 1.1–151 ppm and 0.6–13.30 ppm, respectively. Meanwhile, the La/Lu ratios range from 9 to 76. The spectra also show slight negative or positive Eu anomalies with Eu/Eu* values ranging from 0.2 to 3.2. These anomalies are related to plagioclase fractionation.

The major and minor elements are plotted into the Harker diagrams for oxides to determine their compatibility or relationship with silica. From the Harker diagram for oxides versus SiO_2 (Figure 9), only Al_2O_3 shows a clear negative correlation with SiO_2. As SiO_2 increases, Al_2O_3, CaO, and FeO_{tot} decrease, which would be related to tourmaline fractionation. Al_2O_3 and K_2O decrease with increasing SiO_2, which would be related to the formation of feldspars and muscovite. The dispersion of Na_2O contents in the analyzed samples may be mainly related to their mobility. In fact, two groups of samples can be distinguished for the same SiO_2 values, which would be related to the albite richness. The variation in P_2O_5 would be related to the late apatite fractionation.

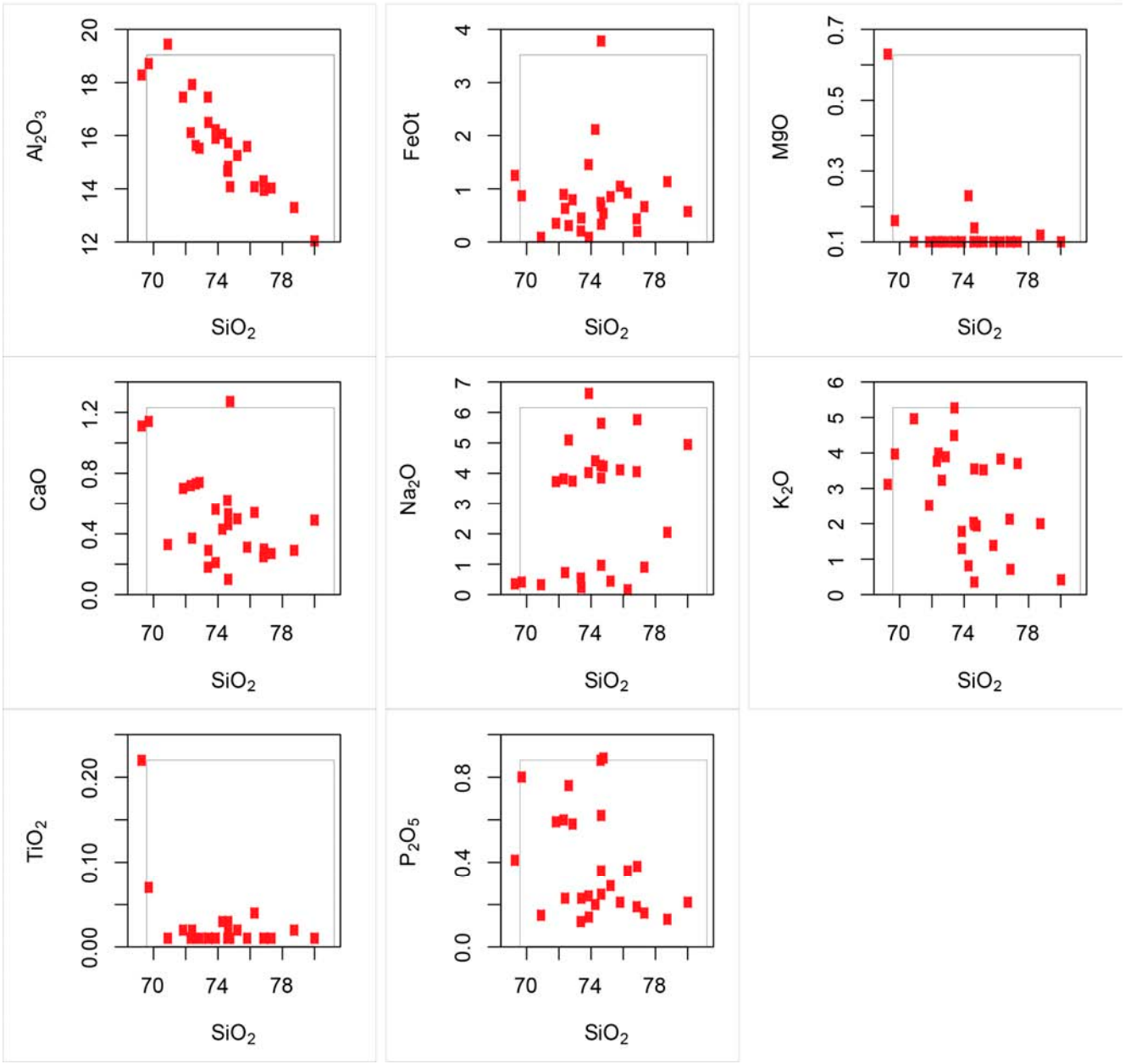

Figure 9. Binary variation diagrams showing major elements versus SiO_2 (wt%) of SBO pegmatites.

On the other hand, trace elements show a strong dispersion (Figure 10). It is possible to observe a very weak negative correlation between silica and Rb, Sr, Y, and Zr; it is even less evident with Ba, Ce, La, and Ni.

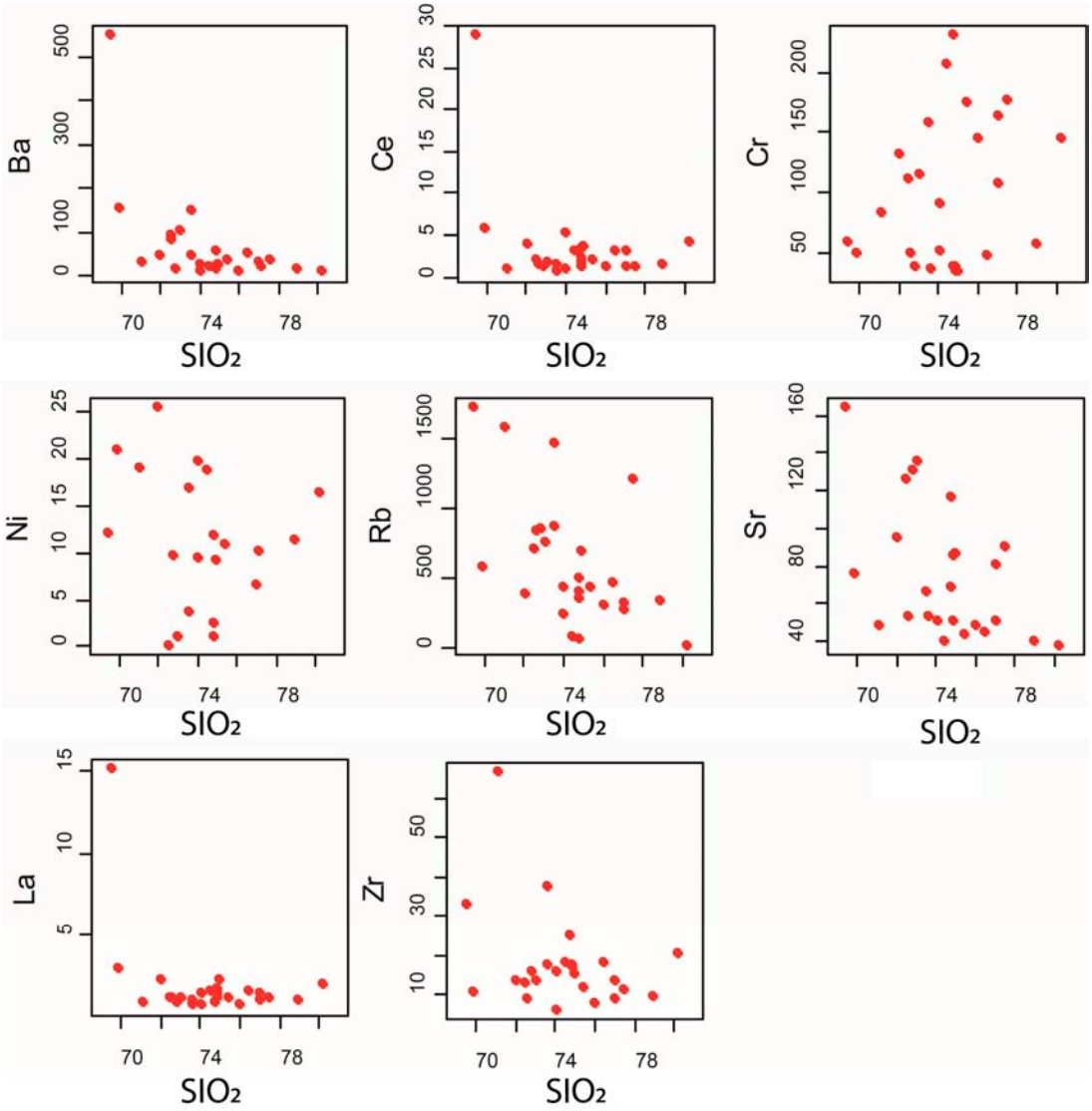

Figure 10. Binary variation diagrams showing trace elements versus SiO2 (wt%) of SBO pegmatites.

5. Discussion

5.1. Geochemical Characteristics of the SBO Pegmatites

5.1.1. Major Elements

The geochemical analysis results have been plotted on a series of diagrams to determine the magmatic characteristics of SBO pegmatites. On the binary ($Na_2O + K_2O$) vs. SiO_2 diagram of Middlemost et al. [51], all samples are plotted within the granite field (Figure 11a).

In the A/NK vs. A/CNK diagram [52], showing $Al_2O_3/(Na_2O + K_2O)$ and $Al_2O_3/(CaO + Na_2O + K_2O)$, respectively, all samples show ratios above 1, reflecting the excess of alumina over Ca, Na, and K. These rocks are therefore peraluminous (Figure 11b), and the aluminum richness is indeed reflected in the mineralogy by the presence of muscovite, together with feldspar, and tourmaline. It is also noted that excess of Al_2O_3 is found as a CIPW normative corundum in many pegmatite samples up to 12.8 wt% (Table 4).

The AFM diagram after Irvine [53], shows calc-alkaline series for SBO pegmatites (Figure 11c).

On the other hand, peraluminous granitic rocks, characterized by high Al contents relative to K, Na, and Ca, are assumed to be derived from the melting of supra-crustal metasedimentary rocks [53]. For Wilson [54] the peraluminous granites contain crustal or

sedimentary material in their magma of origin. This result agrees with the results of the $Al_2O_3/CaO + Na_2O + K_2O$ versus SiO_2 diagram [55], to differentiate between S-type and I-type granites. The SBO pegmatites plot within the S-type granite field (Figure 11d). This type of granitoid implies that the parent magma (from which the pegmatites were formed) contained a large amount of sedimentary or crustal material. This suggests that the SBO pegmatites are derived from the partial melting of the Paleozoic metasedimentary rocks, even though a Precambrian source (not cropping out) is not excluded [23].

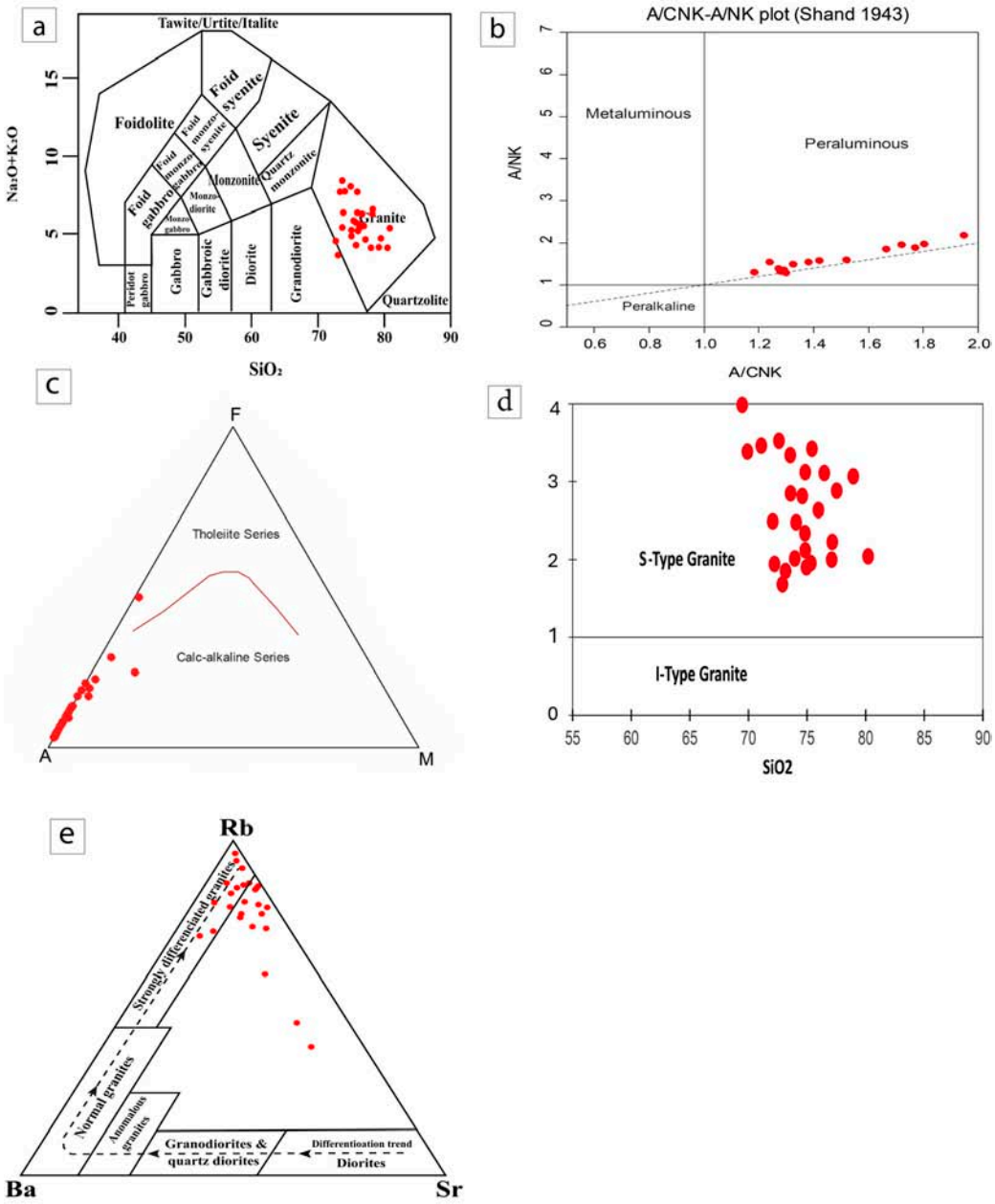

Figure 11. (**a**) Classification diagrams of (SBO) pegmatite TAS diagram (Total Alkalis versus Silica after Middlemost et al. [51]; (**b**) classification diagrams. A/NK versus A/CNK diagram after Maniar et al. [52]; (**c**) AFM diagram after Irvine et al. [53]; (**d**) classification diagrams. $Al_2O_3/CaO + Na_2O + K_2O$ versus SiO_2 after White et al. and Chappell et al. [56,57] (**e**) SBO pegmatite plotted in the Rb-Ba-Sr ternary diagram, after El Bouseily et al. [58].

5.1.2. Minor and Trace Elements

As far as the minor and trace elements, Rb, Sr, and Ba have been plotted in the ternary diagram Rb-Sr-Ba proposed by El Bouseily et al. [58], revealing that the SBO pegmatites occupy the field of strongly differentiated granites (Figure 11e). Some samples also show a relative enrichment in Sr compared to their Ba content. According to El Bouseily et al. [58], Rb, Sr, Ba are monitors of the degree of magmatic differentiation.

In the geodynamic diagram, Rb vs. Nb + Y (proposed by Pearce et al. [59]), pegmatites are plotted in syn-collisional granite, with an exception for volcanic-arc granites (VAG) and within-plate granites (WPG) (Figure 12a). This finding aligns with the Nb vs. Y diagram results after Pearce et al. [59] and Pearce [60], as shown in Figure 12b. There are some deviations observed for within-plate granites (WPG). Similarly, the Rb vs. Yb + Ta diagram shows that all samples are categorized as syn-collisional granite, with a few exceptions being classified as volcanic-arc granites (VAG), as illustrated in (Figure 12c). Additionally, the Ta vs. Yb diagram, following Pearce et al. [58], and the Rb vs. Y/Nb diagram by Pearce et al. [60], further support that all samples have a syn-collisional granite affinity, as demonstrated in Figure 12d.

In the diagram after Batchelor et al. [61] (R1 = 4Si-11(Na + K)-2(Fe + Ti) versus R2 = 6Ca + 2Mg + Al), the SBO pegmatites fall in syn-collisional to post-orogenic for the granite pegmatite field (Figure 12) in syn- collisional (Figure 13).

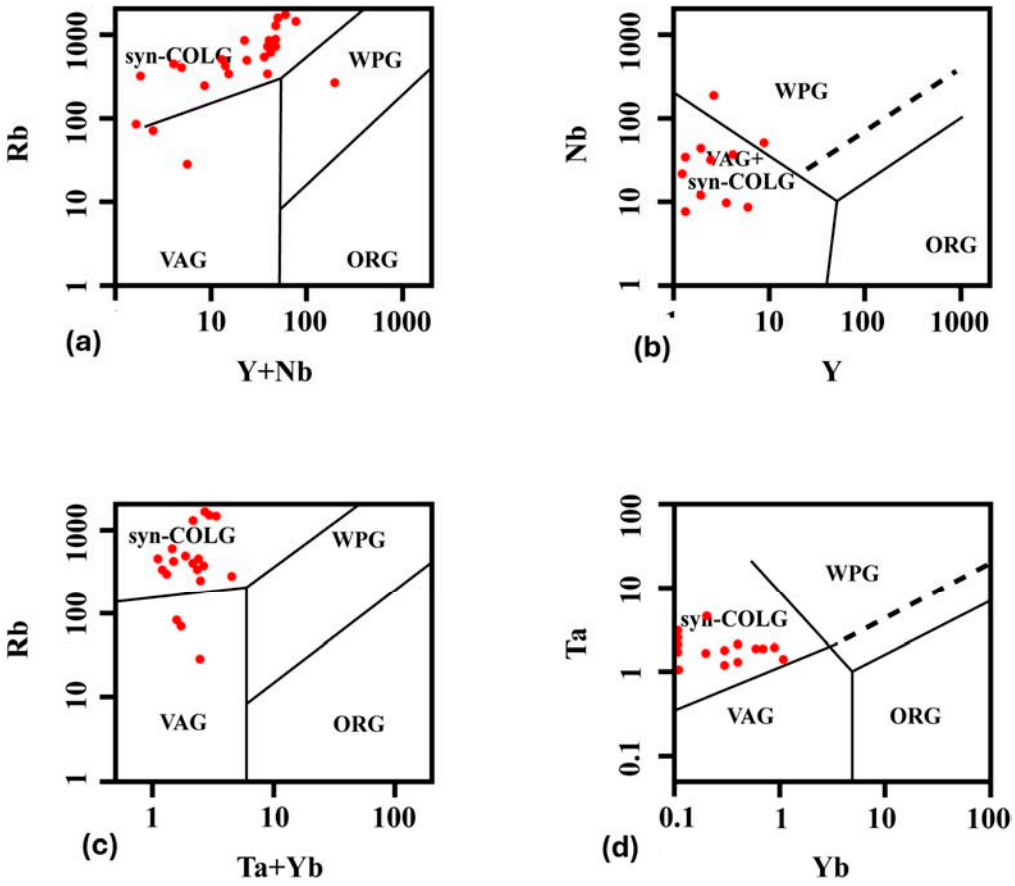

Figure 12. Tectonic discrimination diagrams for SBO pegmatites compositions. (**a**) Rb vs. Y+ Nb diagram; (**b**) Nb vs. Y diagram, after Pearce et al. [59] and Pearce [60]; (**c**) Rb versus Yb + Ta; (**d**) Ta versus Yb, after Pearce et al. [58]. Tectonic fields are ocean-ridge granites (ORG); syn-collisional granites (syn-COLG); volcanic-arc granites (VAG) and within-plate granites (WPG). The SBO pegmatites show syn-collisional granite affinity.

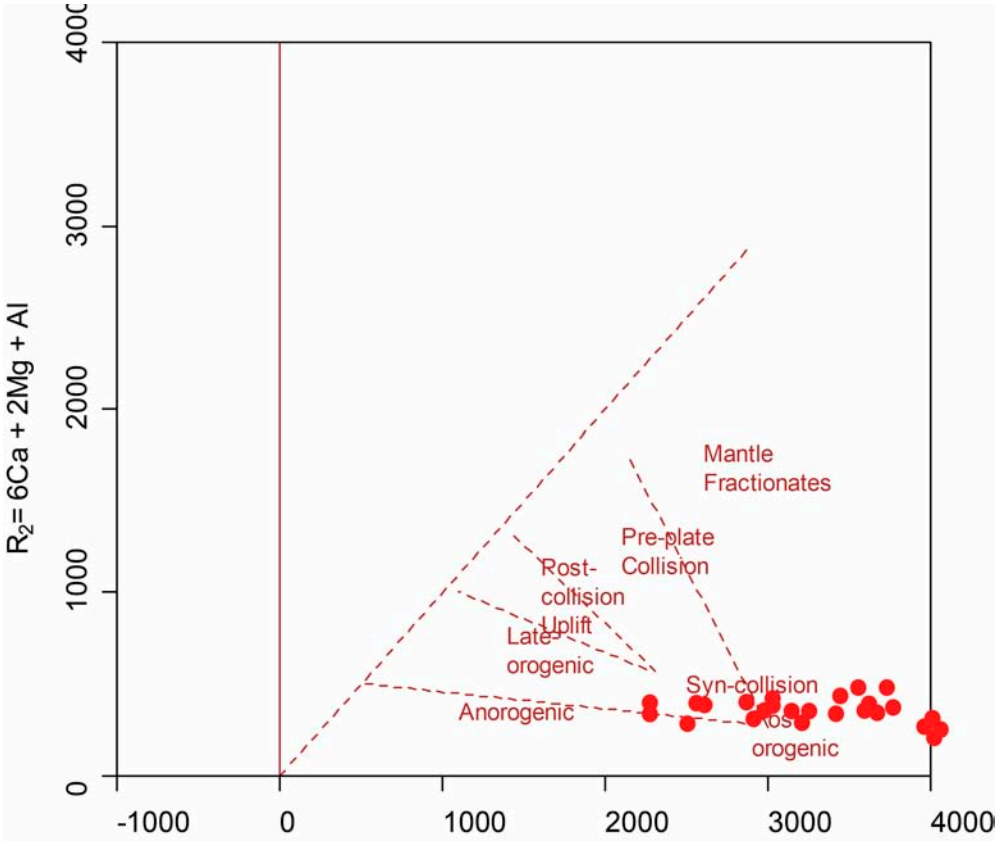

Figure 13. Discrimination geodynamic diagram [59,62] R1 = 4Si-11 (Na + K) −2(Fe + Ti) versus R2 = 6Ca + 2Mg + Al. The SBO pegmatites show syn-collisional and post-orogenic affinity.

The trace element data related to SBO pegmatites samples have been normalized to the upper crust [63]. The multielement diagram (Figure 13) shows strong to moderate positive anomalies in Rb, U, Sr, Sm, and Tm. They sometimes indicate a slight negative anomaly in Nb, Ce, Nd, Zr, and Ti. The negative Nb anomaly represents the role played by magmatic contamination from the continental crust in developing the regional rocks. Negative Nb anomalies are typical of continental crust, while negative Nb and Zr anomalies indicate a calc-alkaline affinity [64].

Negative Ce anomalies are typical of certain orogenic rocks, which Hole et al. [63] and White et al. [64] attribute to an imprint of subducted sediments. However, the quantitative aspect seems to restrict this hypothesis. Ben Othman et al. [65] suggest that the relative Ce deficiency in some orogenic rocks may reflect the specific behavior of this element concerning other REEs during the fluid−rock interactions that take place at subduction zones.

Negative Nb-Ta anomalies and the relative deficit of Nb and Ta compared to light REEs are typical features of rocks associated with subduction zones [65,66]. Some authors attribute this Nb and Ta deficit to selective trapping of these elements by stable titanium mineral phases in the hydrated, high-pressure, high-temperature conditions prevailing at subduction zones [66,67,68,69].

Contrary to a widely held view in the literature, Zr and Hf elements do not show a systematic deficit concerning REEs in orogenic rocks [66]. In this type of representation, positive Zr and Hf anomalies are expressed by ordinate values greater than 1, while negative anomalies are expressed by values less than 1. Thus, orogenic rocks do indeed show both positive and negative Zr and Hf anomalies. In the SBO pegmatite spider diagram, Zr and Hf display negative anomalies.

The spider diagram of the SBO pegmatites shows a good correlation with the patterns for the collision granites calcalkaline type [59]. Some distinctive characteristics are the

high contents of Rb in many of the patterns from the syn-collision granites and the very low contents of Ce and Zr.

The REEs of the SBO pegmatites were normalized to the chondrites of McDonough et al. [70]. The similarity of the rare-earth pattern of the multielement (Figure 14b) suggests a common source for their magmas. The patterns show a relatively weak enrichment in LREEs compared to HREEs. They sometimes show a negative Eu anomaly; at other times, they show a positive Eu anomaly. The pattern of REE spectra agrees with the petrographic observations; for example, the presence of plagioclases is expressed on the REEs spectra with a positive Eu anomaly. The samples show an average enrichment in LREEs. The patterns highlight a good correlation between the REEs distribution and the Eu anomaly. Thus, samples with a positive Eu anomaly have a slightly higher REE concentration.

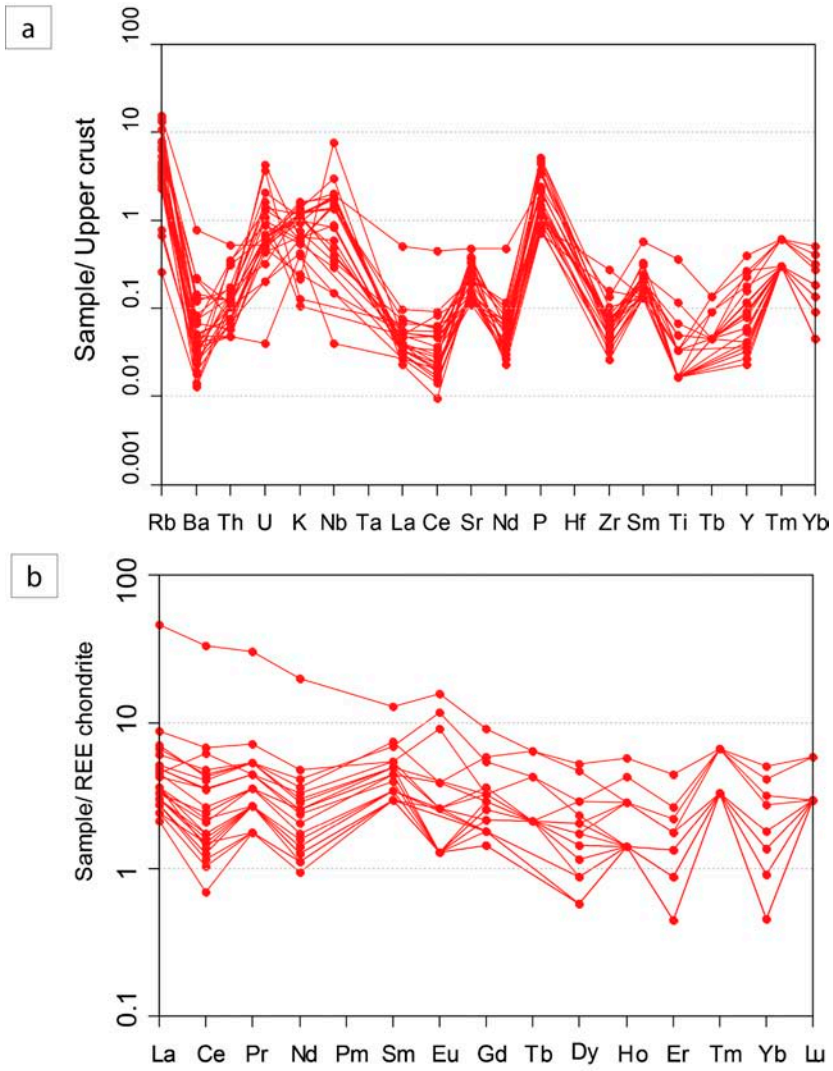

Figure 14. Multielement spider and REEs normalization diagrams explaining magma source and differentiation: (**a**) Upper Continental Crust spider plot normalized and (**b**) REE chondrite spider plot after McDonough et al. [70].

5.2. Hydrothermal Alteration and Metasomatism

In addition to providing information on the physicochemical conditions of the system, the distribution of trace elements and EARs in the SBO pegmatites revealed important information on the rock/fluid interaction (Figure 15). Due to the dissolution or replacement of primary and accessory minerals and the consequent development of new

mineral phases, virtually all trace elements were mobilized during hydrothermal alteration, and the petrographic study indeed confirms these changes. Moreover, the different types of hydrothermal alteration that affected these pegmatites can also be characterized using several geochemical diagrams proposed in the literature. The diagram of Stemprok [71] using the normative composition Qz-Ab-Or allows us to determine the sodic, potassic, silicic, and greisen alterations. The pegmatite samples are distributed in fields indicating silicification and greisinization, respectively (Figure 15).

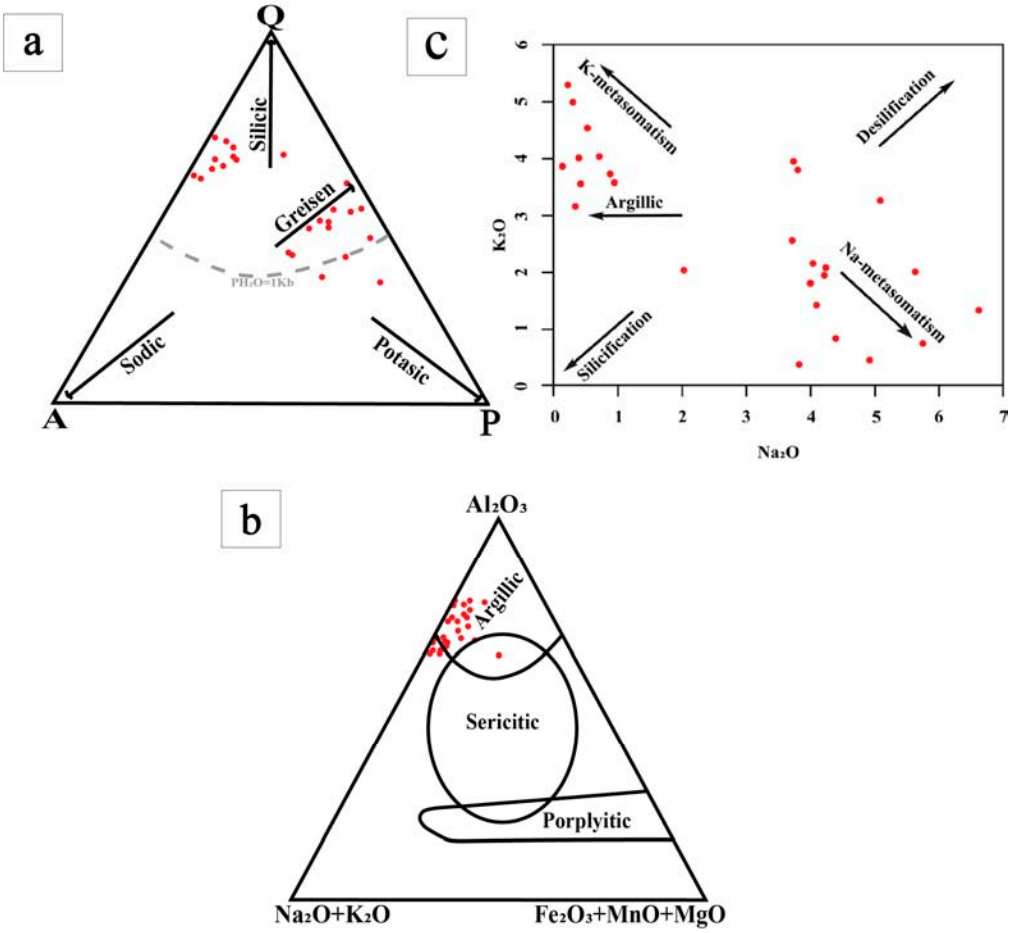

Figure 15. (**a**) Ternary diagrams showing Normative Qz-Ab-Or ternary diagram [71]; (**b**) bivariate K_2O − Na_2O variation diagram [49]; (**c**) Al_2O_3 − (Na_2O + K_2O) − (Fe_2O_3 t +MnO + MgO) ternary diagram showing alteration type [72].

These results are confirmed by microscopic observations where the occurrence of quartz and the quartz−muscovite association from the transformation of minerals of the primary paragenesis is evident. However, additional samples display considerable Na_2O levels and tend to albite composition. Albitization occurs during sodium metasomatism when Na^+ substitutes for K^+ and Ca^{2+} in pre-existing feldspars. The silicification leads to an increase in SiO_2 at the expense of the other major oxides and is followed by an increase in a few trace elements, including Zr, Ba, and Rb. The K_2O vs. Na_2O diagram of Cuney et al. [48] shows that these pegmatites are affected by mainly clay sodic and potassic alterations (Figure 15c).

Moreover, the argillic alteration is the most dominant and marked (Figure 15b) according to the ternary diagrams Al_2O_3 − (Na_2O + CaO) − K_2O and Al_2O_3 − (Na_2O + K_2O) − (Fe_2O_3t + MnO + MgO) and of Meyer and at., [73].

The action of hydrothermal fluids was intense and generalized to all the pegmatitic bodies as suggested by Fransolet [12] and confirmed by Fontan [23].

5.3. Classification

The current schemes used to classify pegmatites are varied as well as numerous. Several authors have proposed different classification schemes based on the typical and auxiliary minerals of the pegmatite, on the P-T conditions of its emplacement, and, more recently, on its geochemistry [23,26,74,75]. However, the classification of pegmatites by Ginsburg et al. [76] has had a significant influence on contemporary methods of pegmatite classification. This classification groups the pegmatites according to their depth of emplacement, association with metamorphism, and relationship to granitic plutons. The currently used taxonomy of pegmatites has the support of researchers and is known as the revision of Černy [77,78]. Its classification is based on a combination of minor element concentration and metamorphic grade at depth of emplacement. The four main classes or types are identified as follows: (1) Abysal (AB) is the high-grade temperature (700–800 °C), high to low pressure (4–9 kbar) and depth ≥ 11 km; (2) Muscovite (MSC) is a lower temperature (580–650 °C) high pressure (5–8 kbar) and depth (7–11 km); (3) Rare-Element (REL) is a low temperature (500–650 °C) and pressure (2–4 kbar) and depth (3.5–7 km); (4) Miarolitic (MI) is a shallow level 500–650 °C at low temperature (≤500 °C) and pressure (1–2 kbar) and depth (1.5–3.5 km).

The SBO pegmatite study highlights that these rocks are essentially composed of large crystals of feldspar, quartz, muscovite and (occasionally) tourmaline. They are hosted exclusively in schists, and no outcrops of granite have been observed in this area. Moreover, the geochemical results of these rocks indicate that they do not present any significant enrichment and that they are poor in REEs; however, on the other hand, they are quite famous for their content in ceramic minerals [20]. These characteristics allow us to classify the SBO pegmatites in the class of muscovite pegmatites. According to Černy [77], the latter are rarely mineralized but can produce feldspars and muscovite. They are of metamorphic origin, characterized by high-pressure metamorphism, hosted in almandine and kyanite schists, and they may contain Th, U, Nb, Ta, Zr, Ti [7,78]. Direct anatexis is thought to be the origin of first-drop rare-element mineralised pegmatites [79] and could also explain the diversity of magmatic fractionation observed in each type of pegmatite [79]. The crustal anatexis model was suggested in the 1970s [80–84] to justify the extent of pegmatite fields compared with that of granitic plutons [85]. It has also been used to justify (i) the absence of granite related to LCT pegmatite fields, (ii) the diachronism between granites and pegmatites [85], and (iii) the lack of continuity of magmatic fractionation between granites and the most differentiated pegmatites [86,87]. Furthermore, the diversity of mineralization and geochemical signatures associated with the pegmatite complex is mainly linked to the P-T conditions of regional metamorphism rather than to the fractional crystallization of granitic bodies during their crystallization [88].

5.4. Origin of SBO Pegmatites

The most widely accepted model for the genesis of pegmatites in the 1970s and 1980s was fractional crystallization of a granitic fluid. However, it is becoming accepted that they can be formed by metamorphic rock anatexis [88]. Considering the different models proposed that simplify the formation and mineralization of pegmatites, the following two final models have been proposed for pegmatite formation: the continuous crystallization and the fractional dissolution [89].

According to Shmakin et al. [90], Gorlov [91], and Sokolov et al. [92], pegmatites of the muscovite class are produced directly by partial melting or by a very limited level of differentiation of anchiautochthonic palingenitic granites [78,92–94]. This suggests that SBO pegmatites resulted from the partial melting of the argillaceous metasedimentary rock of Sarhlef shist during Varsican subduction and shortening. This corroborates the geodynamic models proposed to explain the evolution of the Meseta from Upper Devonian to Lower Permian. The eastward subduction of the Rheic Ocean, leading to the

formation of fore- and back-arc basins in the Mesetian block between the 420 and 330 Ma models [40,95,96], corroborates the Evolution model of the Meseta during the Carboniferous proposed by Essaifi et al. [97], which involves westward subduction followed by a slab breakoff, leading to upwelling of hot asthenospheric currents and eroding the litho-sphere.

6. Conclusions and Final Remarks

The SBO Variscan pegmatite crop out as dykes mainly oriented N30° (N-S to NNE-SSW) with sub-vertical dip. The field investigations show that E-W dykes are secant on NS pegmatite dykes. Their thicknesses vary from centimeters to meters (30 cm to 8 m), and they have extensions ranging from 1 m to 500 m. These dykes underwent a deformation presented on the ground by boudinage, and strike-slip faults shifted their architectures.

SBO pegmatites are observed within the metamorphic rocks of the Sarlef series. They are clearly delimited bodies, which are mainly zoned and rarely homogeneous. They are never isolated; rather, they are in a group of several dykes which are organized in clusters. SBO pegmatites show clearly tectonic control and are syn- or tardi-orogenic, have a calco-alkalic affinity, and are composed of S-type granite. Using the mineralogy and the geochemistry, these pegmatites fall into a very strongly differentiated granite field. Their geochemical features are compatible with their petrographic and mineralogical characteristics. They are mainly constituted by quartz, albite, muscovite, and tourmaline, with minor amounts of microcline and illite and accessories such as garnet, apatite, and zircon. These characteristics allow us to classify the SBO pegmatites in the class of muscovite pegmatites. The classification of the SBO pegmatites within this class indicates that they do not present any significant enrichment in REEs. They are probably the products of the partial melting of pelitic metasedimentary rock of Sarhlef during Varsican shortening between 330 and 280–275 Ma, even though a contribution of older formations is not excluded.

Finally, in the frame of the shift to green technologies, it is worth noting that, apart from some accessory minerals of interest that are hosted in pegmatite-type deposits, some main occurring minerals, such as feldspars and quartz, are increasingly required for the production and storage of renewable (green) energy to supply the green and sustainable societies of the future [88]. For instance, feldspars have been recently assessed by the European Commission as being critical raw materials (CRMs) (https://single-market-economy.ec.europa.eu/publications/study-critical-raw-materials-eu-2023-final-report_en (accessed on 31 October 2023)).

Therefore, in the frame of the current global trend, the SBO pegmatite may constitute an important resource to be considered in greater detail.

Author Contributions: Conceptualization, A.W.; methodology, A.W.; software, N.E.A., Y.M. and M.C.; validation, A.W., Y.M. and M.C.; formal analysis, A.W.; investigation, A.W., M.C. and W.A.S.; resources, A.W.; data curation, A.W., M.C. and W.A.S.; writing—original draft preparation, A.W., Y.M., R.P., D.G. and A.M.C.; writing—review and editing, A.W., R.P., D.G. and A.M.C.; visualization, A.W.; supervision, A.W.; project administration, A.W.; funding acquisition, Y.D. All authors have read and agreed to the published version of the manuscript.

Funding: This research received no external funding.

Data Availability Statement: The data is included in the article.

Acknowledgments: We acknowledge Reminex, Managem Group for ICP-MS analysis.

Conflicts of Interest: The authors declare no conflicts of interest.

References

1. London, D. Pegmatites. *Can. Mineral. Spec. Publ.* **2008**, *10*, 1–347.

2. London, D. The origin of primary textures in granitic pegmatites. *Can. Mineral.* **2009**, *47*, 697–724. https://doi.org/10.3749/canmin.47.4.697.
3. London, D. Crystal-filled cavities in granitic pegmatites: Bursting the bubble. *Rocks Miner.* **2013**, *88*, 527–538.
4. Steiner, B.M. Tools, and workflows for grassroots Li-Cs-Ta (LCT) pegmatite exploration. *Minerals* **2019**, *9*, 24–26.
5. Linnen, R.L.; Van Lichtervelde, M.; Černý, P. Granitic Pegmatites as Sources of Strategic Metals. *Elements* **2012**, *8*, 275–280. https://doi.org/10.2113/gselements.8.4.275.
6. London, D. A petrologic assessment of internal zonation in granitic pegmatites. *Lithos* **2014**, *184*, 74–104.
7. London, D. Ore-forming processes within granitic pegmatites. *Ore Geol. Rev.* **2018**, *101*, 349–383.
8. Bouladon, J.; Jouravsky, G.; Morin, P. Etude préliminaire des pegmatites a muscovite et béryl du Sud de la Plaine de Tazenakht. *Notes Mem. Serv. Geol. Maroc* **1950**, *3*, 207–235.
9. Bouladon, J.; Jouravsky, G.; Vergerto, R. Note sur les recherches de béryl et de mica dans le Sud de la plaine de Tazenakht. *Rapp. Serv. Géol. Maroc Div. Serv. Etudes Gîtes* **1952**, *6*, 297.
10. Permingeat, F. Sur les niobo-tantalates de l'Anti-Atlas, Maroc: Tapiolite et columbite. *Bull. Soc. Fr. Mineral. Cristallogr.* **1955**, *78*, 123–156.
11. Cech, F.; Johan, Z.; Povondra, P. La barbosalite de la pegmahte d'Angarf-Sud,Plaine de Tazenakht, Anti-Atlas, Maroc. *Notes Serv. Geol. Maroc* **1972**, *32*, 121–128.
12. Fransolet, A.M. Les phosphates lithiques des pegmatites de la Plaine des Zenaga (Anti-Atlas, Maroc). *Notes Serv Geol. Maroc* **1974**, *35*, 137–143.
13. Fransolet, A.M.; Antenucci, D.; Speetjens, J.M.; Tarte, P. An X-ray determinative method for the divalent cation ratio in the triphylite-lithiophilite series. *Mineral. Mag.* **1984**, *48*, 373–381.
14. Fransolet, A.M.; Abraham, K.; Speetjens, J.M. Evolution génétique et signification des associations de phosphates de la pegmatite d'Angarf-Sud, plaine de Tazenakht, Anti-Atlas, Maroc. *Bull. Minér.* **1985**, *108*, 551–574.
15. Kampf, A.; Mills, S. ANGARFITE, $NaFe^{3+}{}_5(PO_4)_4(OH)_4 \bullet 4H_2O$, a new mineral species from the Angarf-sud pegmatite, Morocco: Description and crystal structure. *Can. Mineral.* **2012**, *50*, 781–791.
16. Morsly, Y.; Zerhouni, Y.; Maimouni, S.; Alikouss, S.; Kadir, H. Pegmatite mapping using spectroradiometry and ASTER data (Zenaga, Central Anti-Atlas, Morocco). *J. Afr. Earth Sci.* **2021**, *177*, 104–173. https://doi.org/10.1016/j.jafrearsci.2021.104153.
17. Morsli, Y.; Zerhouni, Y.; Wafik, A.; Elouazzani, A.; Alikouss, S.; Saidi, A.; Baroudi, Z. Eburneen pegmatites of the Zenaga inlier (Anti-Atlas, Morocco): Petrography, geochemistry, and classification. *J. African Earth Sci.* **2022**, *186*, 104–438. https://doi.org/10.1016/j.jafrearsci.2021.104438.
18. Permingeat, F. Presence du lithium dans les pegmatites de Sidi Bou Othmane (Jebilet). *Mines Geol.* **1959**, *8*, 46–47.
19. Huevelin, P.; Mazeas, J. Presence de cassiterite et de beryl dans les pegmatites hercyniennes de la region de Sidi Bou Othmane (Jebilet centrales, Maroc). *C. R. Somm. Soc. Geol. Fr.* **1964**, *10*, 419–420.
20. Agard, J.; Morin, P. Beryllium et mica. *Notes Serv. Geol. Maroc* **1980**, *276*, 257–269.
21. Fontan, F.; Huvelin, P.; Permingeat, F. Rockbridgeite, phosphosiderite et mitridatite des pegmatites de Sidi Bou Othmane (Jebilet). *Notes Serv. Geol. Maroc* **1972**, *32*, 150–151.
22. Fontan, F. Phosphates mineurs des pegmatites de Sidi Bou Othmane. *Notes Serv. Geol. Maroc* **1975**, *40*, 249–252.
23. Fontan, F.; Huvelin, P.; Orliac, M.; Permingeat, F. La ferrisicklerite des pegmatites de Sidi Bou Othmane (Jebilet, Maroc) et le groupe des mineraux astructure de triphylite. *Bull. Soc. Fr. Mineral Cristallogr*. **1976**, *99*, 274–286.
24. Essafi, A.; Lacinska, A.M.; Corsini, M.; Goodenough, K.M.; Arbaoui, A.E.; Zayane, R. Mobilisation of rare earth elements in shear zones: Insights from the Tabouchent granodioritic pluton (Jebilet massif, Variscan Belt, Morocco). *Ore Geol. Rev.* **2021**, *133*, 103996. https://doi.org/10.1016/j.oregeorev. 2021.103996.
25. Bouloton, J.; Gasquet, D. Melting and undercooled crystallisation of felsic xenoliths from minor intrusions (Jebilet massif, Morocco). *Lithos* **1995**, *35*, 201–219.
26. Delchini, S.; Lahfid, A.; Lacroix, B.; Baudin, T.; Hoepffner, C.; Guerrot, C.; Lach, P.; Saddiqi, O.; Ramboz, C. The geological evolution of the Variscan Jebilet massif, Morocco, inferred from new structural and geochronological analyses. *Tectonics* **2018**, *37*, 4470–4493.
27. Zouicha, A.; Saber, H.; Attari, A.E.; Zouheir, T.; Ronchi, A. Late Hercynian tectonic evolution of the Jebilet Massif (Western Meseta, Morocco) based on tectono-sedimentary analyses of related Permian continental deposits. *J. Iber. Geol.* **2022**, *48*, 377–403.
28. Huvelin, P. Etude géologique et gîtologique du Massif hercynien des Jebilet (Maroc occidental). *Notes Mém. Serv. Géol. Maroc* **1977**, *232*, 1–307.
29. Lazreq, N.; Königshof, P.; Essaifi, A.; Bouari, A.; Outigua, A. A Devonian age for the Sarhlef Formation (Jebilet Massif, Morocco)—Evidence from new biostratigraphic data based on metamorphosed conodonts. *Palaeogeogr. Palaeoclimatol. Palaeoecol.* **2021**, *572*, 110395. https://doi.org/10.1016/j.palaeo.2021.110395.
30. Bordonaro, M. Tectonique et pétrographie du district à pyrrhotine de Kettara. Ph.D. Thesis, Univ. Louis-Pasteur, Strasbourg, France, 1983.
31. Lagarde, J.L.; Ait Omar, S.; Roddaz, B. Structural characteristics of granitic plutons emplaced during weak regional deformation: Examples from late Carboniferous plutons, Morocco. *J. Struct. Geol.* **1990**, *12*, 805–821. https://doi.org/10.1016/0191-8141(90)90056-5.

32. Pique, A.; Michard, A. Moroccan Hercynides: A synopsis. The Paleozoic sedimentary and tectonic evolution at the northern margin of West Africa. *Am. J. Sci.* **1989**, *289*, 286–330. https://doi.org/10.2475/ajs.289.3.286.
33. Michard, A.; Driouch, Y.; Kuiper, Y.D.; Caby, R.; Farah, A.; Ouanaimi, H.; Soulaimani, A.; Chabou, M.C.; Saddiqi, O. The Variscan belts of North-West Africa: An African legacy to the Wilson Cycle concept. *J. Afr. Earth Sci.* **2023**, *208*, 105042. https://doi.org/10.1016/j.jafrearsci.2023.105042.
34. El Hassani, I.E.E.A. Petrogenèse des granitoïdes peralumineux des Jebilet centrales (Maroc) approche par l'étude des enclaves. *Bull. L'inst. Sci.* **1996**, *20*, 1–23.
35. Chopin, F.; Leprêtre, R.; el Houicha, M.; Tabaud, A.S.; Schulmann, K.; Míková, J.; Barbarand, J.; Chebli, R. U–Pb geochronology of Variscan granitoids from the Moroccan Meseta (Northwest Africa): Tectonic implications. *Gondwana Res.* **2023**, *117*, 274–294. https://doi.org/10.1016/j.gr.2023.02.004.
36. Bouloton, J. Mise en évidence de cordiérite héritée des terrains traversés dans le pluton granitique des Oulad Ouaslam (Jebilet, Maroc). *Can. J. Earth Sci.* **1992**, *29*, 658–668.
37. Mrini, Z.; Rafi, A.; Duthou, J.; Vidal, P. Chronologie Rb-Sr des granitoïdes hercyniens du Maroc : Conséquences. *Bull. Soc. Geol. Fr.* **1992**, *163*, 281–291.
38. Gaillet, J.; Bordonaro, M. La tectogenèse hercynienne dans le massif dinantien des Jebilet centrales (Maroc). *Sci. Géologiques Bull.* **1981**, *34*, 117–122. https://doi.org/10.3406/sgeol.1981.1595.
39. Bouloton, J.; Gasquet, D.; Pin, C. Petrogenesis of the Early-Triassic quartz-monzodiorite dykes from Central Jebilet (Moroccan Meseta): Trace element and Nd-Sr isotope constraints on magma sources, and inferences on their geodynamic context. *J. Afr. Earth Sci.* **2019**, *149*, 451–464.
40. Michard, A.; Soulaimani, A.; Hoepffner, C.; Ouanaimi, H.; Baidder, L.; Rjimati, E.C.; Saddiqi, O. The South-Western Branch of the Variscan Belt: Evidence from Morocco. *Tectonophysics* **2010**, *492*, 1–24.
41. Bouloton, J.; Le Corre, C. Le problème de la tectonique tangentielle dans les Jebilet (Maroc hercynien): Données et hypothèses. *Hercynica* **1985**, *1*, 121–129.
42. Lagarde, J.L.; Ait Ayad, N.; Ait Omar, S.; Chemsseddoha, A.; Saquaque, A. Les plutons granitiques tardi carbonifères marqueurs de la déformation crustale. L'exemple des granitoïdes de la méseta marocaine. *Comptes Rendus l'Acad. Sci.* **1989**, *309*, 291–296.
43. El Mostadi, A. Etudes Géologique, Pétrographique et Gitologique des Skarns Minéralisés en Scheelite et Cassitérite du Secteur de Sidi Bou Othmane (Jebilet Centrales, MAROC) Guides de Recherches. Ph.D. Thesis, Université Cadi Ayyad Faculté des Sciences Marrakech, 1992.
44. Beauchamp, J.; Izart, A. Early Carboniferous basins of the Atlas-Meseta domain (Morocco): Sedimentary model and geodynamic evolution. *Geology* **1987**, *15*, 797–800. https://doi.org/10.1130/0091-7613(1987)15<797:ECBOTA>2.0.CO;2.
45. Hanson, G. The application of trace elements to the petrogenesis of igneous rocks of granitic composition. *Earth Planet. Sci. Lett.* **1978**, *38*, 26–43.
46. Lagarde, J.L.; Choukroune, P. Cisaillement ductile et granitoides syntectoniques; l'exemple du Massif Hercynien des Jebilet (Maroc). *B. Soc. Geol. Fr.* **1982**, *7*, 299–307.
47. Herrmann, A.G. Yttrium, and lanthanides. In *Handbook of Geochemistry*; Wedepohl, K.H., Eds; Springer: Berlin, Germany, 1970; Volume 2, pp. 39–57.
48. Hulsbosch, N.; Hertogen, J.; Dewaele, S.; André, L.; Muchez, P. Alkali metal and rare earth element evolution of rock-forming minerals from the Gatumba area pegmatites (Rwanda): Quantitative assessment of crystal-melt fractionation in the regional zonation of pegmatite groups. *Geochim. Et Cosmochim. Acta* **2014**, *132*, 349–374. ISSN 0016-7037. https://doi.org/10.1016/j.gca.2014.02.006.).
49. Cuney, M.; Friederich, M. Physicochemical and crystal-chemical controls on accessory mineral paragenesis in granitoids: Implications for uranium metallogenesis. *Bull. Minéral* **1987**, *110*, 235–47. https://doi.org/10.3406/bulmi.1987.7983.
50. Chatelineau, M. U-Th-RRE mobility during albitization and quartz dissolution in granitoids: Evidence from southeast French Massif Central. *Bull. Mineral.* **1987**, *110*, 249–259. https://doi.org/10.3406/bulmi.1987.7984.
51. Middlemost, E.A.; Magmas, K.; Rocks, M. An introduction to igneous petrology. In *Magma and Magmatic Rocks*; Longman Group Ltd.: London, UK, 1985; pp. 1–266.
52. Maniar, P.D.; Piccoli, P.M. Tectonic discrimination of granitoids. *Geol. Soc. Am. Bull.* **1989**, *101*, 635–643.
53. Irvine, T.N.; Baragar, W.R.A. A Guide to the Chemical Classification of the Common Volcanic Rocks. *Can. J. Earth Sci.* **1971**, *8*, 523–548.
54. Barbarin, B. Genesis of the two main types of peraluminous granitoids. *Geology* **1985**, *24*, 295–298.
55. Wilson, M. *Igneous Petrogenesis Global Tectonic Approach*, 1st ed.; Harpar Collins Academy: London, UK, 1989; pp. 227–241.
56. White, R.J.A.; Chappell, W.B. Ultrametamorphism and Granitoid Genesis. *Tectonophysics* **1977**, *43*, 7–22. https://doi.org/10.1016/0040-1951(77)90003-8.
57. Chappell, B.; White, A.J. Two contrasting granite types. *Pacif. Geol.* **1974**, *8*, 173–174.
58. El Bousely, A.; El Sokkary, A. The relation between Rb, Ba, and Sr in granitic rocks. *Chem. Geol.* **1975**, *16*, 207–219.
59. Pearce, J.; Harris, N.; Tindle, A. Trace element discrimination diagrams for the tectonic interpretation of granitic rocks. *J. Petrol.* **1984**, *25*, 956–983.
60. Pearce, J.A. A User's Guide to Basalt Discrimination Diagrams. In *Trace Element Geochemistry of Volcanic Rocks: Applications for Massive Sulphide Exploration;* Wyman, D.A., Ed.; Geological Association of Canada, Short Course Notes**, 1996**; *12*, pp. 79–113.

61. Batchelor, R.; Bowden, P. Petrogenetic interpretation of granitoid rock series using multicationic parameters. *Chem. Geol.* **1985**, *48*, 43–55.
62. Taylor, S.R.; McLennan, S.M. The geochemical the continental evolution crust. *Rev Mineral Geochem* **1995**, *33*, 241–265.
63. Hole, M.J.; Saunders, A.D.; Marriner, G.F.; Tarney, J. Subduction of pelagic sediments: Implications for the origin of Ce-anomalous basalts from the Mariana Islands. *J. Geol. Soc.* **1984**, *141*, 453–472. https://doi.org/10.1144/gsjgs.141.3.0453.
64. White, W.M.; Patchett, J. Hf Nd Sr isotopes and incompatible element abundances in island arcs: Implications for magma origins and crust-mantle evolution. *Earth Planet. Sci. Lett.* **1984**, *67*, 167–185. https://doi.org/10.1016/0012-821X(84)90112-2.
65. Ben Othman, D.; White, W.; Patchett, J. The geochemistry of marine sediments, island arc magma genesis, and crust-mantle recycling. *Earth Planet. Sci. Lett.* **1989**, *94*, 1–21.
66. Briqueu, L.; Bougault, H.; Joron, J.L. Quantification of Nb, Ta, Ti and V anomalies in magmas associated with subduction zones: Petrogenetic implications. *Earth Planet. Sci. Lett.* **1984**, *68*, 297–308. https://doi.org/10.1016/0012-821X(84)90161-4.
67. Wood, D.A. A variability veined sub-oceanic upper mantle-genetic significance for mid-ocean ridge basalts from geochemical evidence. *Geology* **1979**, *7*, 499–503.
68. Morris, J.D.; Hart, S.R. Isotopic and incompatible element constraints on the genesis of island arc volcanics from Cold Bay and Amak Island, Aleutians, and implications for mantle structure: Reply to a Critical Comment by M. R. Perfit and R. W. Kay. *Geochim. Cosmochim. Acta* **1983**, *50*, 483–487. https://doi.org/10.1016/0016-7037(86)90202-4.
69. Saunders, A.D.; Tarney, J.; Weaver, S.D. Transverse geochemical variations across the Antarctic Peninsula: Implications for the genesis of calc-alkaline magmas. *Earth Planet. Sci. Lett.* **1980**, *46*, 344–360. https://doi.org/10.1016/0012-821X(80)90050-3.
70. Mc Donough, W.; Sun, S. The composition of the Earth. *Chem. Geol.* **1995**, *120*, 223–253.
71. Stemprok, M. Mineralized granites and their origin: Review of MAWAM contributions. *Episodes* **1979**, *12*, 49–53. https://doi.org/10.18814/epiiugs/1979/v2i3/005.
72. Nasbitt, H.W.; Young, G.M. Formation and diagenesis of weathering profiles. *J. Geol.* **1989**, *97*, 129–147. https://doi.org/10.1086/629290.
73. Meyer, C.; Hemely, J.J. *Wall Rock Alteration in Geochemistry of Ore Deposits*; Barnes, H.L., Ed.; Holt, Ranehart & Winston: New York, NY, USA, 1967; pp. 166–235.
74. Wise, M.A.; Müller, A.; Simmons, W.B. A proposed new mineralogical classification system for granitic pegmatites. *Can. Mineral.* **2022**, *60*, 229–248.
75. Simmons, W.B. A look at pegmatite classifications. In Proceedings of Crystallization Processes in Granitic Pegmatites-International Meeting, Elba Island, Italy, 23–29 May 2005.
76. Ginsburg, A.; Timofeyev, I.; Feldman, L. *Principles of Geology of the Granitic Pegmatites*. Nedra: Moscow, Russia, 1979; p. 296.
77. Černý, P.; Ercit, T.S. The classification of granitic pegmatites revisited. *Can. Mineral.* **2005**, *43*, 2005–2026.
78. Simmons, W.B.S.; Webber, K.L. Pegmatite genesis: State of the art. *Eur. J. Mineral.* **2008**, *20*, 421–438.
79. Černy, P. Rare-element granitic pegmatites. Part II: Regional to global environments and petrogenesis. *Geosci. Canada* **1991,** *18*. Available online: https://journals.lib.unb.ca/index.php/GC/article/view/3723 (accessed on 1 October 2023).
80. Roda-Robles, E.; Pesquera, A.; Velasco, F.; Fontan, F. The granitic pegmatites of the Fregeneda area (Salamanca, Spain): Characteristics and petrogenesis. *Mineral. Mag.* **1999**, *63*, 535–558.
81. Norton, J.J. Composition of a pegmatite. *Am. Mineral.* **1970**, *55*, 981—1002.
82. Zasedatel, A.M. Possible accumulation oflithium in host rocks of lithium pegmatite veins during old sedirnentation processes. *Dokl. Acad. Sci. USSR Earth-Sci.Sect.* **1974**, *218*, 196–198.
83. Zasedatel, A.M. Quantitative model of metamorphic generation of rare-metal pegmatite with lithium mineralization. *Dokl. Acad. Sci. USSR Earth-Sci.Sect.* **1977**, *236*, 219–221.
84. Stewart, D.B. Petrogenesis of lithium-rich pegmatites. *Am. Mineral*. **1978**, *63*, 970—980.
85. Norton, J.J.; Redden, J.A. Relations of zoned pegmatites to other pegmatites,granite,and metamorphic rocks in the southernBlack Hills, SouthDakota. *Am. Mineral.* **1990**, *75*, 631—655.
86. Melleton, J.; Gloaguen, E.; Frei, D.; Novák, M.; Breiter, K. How are the emplacement of rare-element pegmatites, regional metamorphism and magmatism interrelated in the Moldanubian domain of the Variscan Bohemian Massif, Czech Republic? *Can. Mineral.* **2012**, *50*, 1751–1773.
87. Martins, T.; Lima, A.; Simmons, W.B.; Falster, A.; Noronha, F. Geochemical fractionation of Nb–Ta oxides in li-bearing pegmatites from the Barroso–Alvão pegmatite field, northern Portugal. *Can. Mineral.* **2011**, *49*, 777–791.
88. Nabelek, P.I.; Russ-Nabelek, C.; Denison, J.R. The generation and crystallization conditions of the Proterozoic Harney Peak Leucogranite, Black Hills, South Dakota, USA: Petrologic and geochemical constraints. *Contrib. Mineral. Petrol.* **1992**, *110*, 173–191.
89. Simmons, W.B.; Foorf, E.E.; Falster, A.U.; King, V.T. Evidence for an anatectic origin of granitic pegmatites, western Maine, USA. *Geol. Soc. Am. Bull.* **1995**, *27*, 411.
90. Shmakin, B.M.; Makagon, V.M. Physicochemical conditions of formation of the muscovite-bearing pegmatites. *Proc. Int. Geol. Congr.* **1972**, *3*, 591–599.
91. Gorlov, N.V. Structural principles of exploration for pegmatite deposits in northwestern White Sea region. In *Muscovite Pegmatites of the USSR*; Nauka: Leningrad, Russia, 1975; pp. 146–153.

92. Sokolov, Y.M.; Kratz, K.O.; Glebovitskyi, V.A. Regularities in the formation and distribution of the muscovite and muscovite—Rare metal pegmatite formations in metamorphic belts. In *Muscovite Pegmatites of the USSR*; Nauka: Leningrad, Russia, 1975; pp. 5–15.
93. Bushev, A.G. Linkage of muscovite pegmatites with granites. In *Muscovite Pegmatites of the USSR*; Nauka: Leningrad, Russia, 1975; pp. 77–84.
94. Gordiyenko, V.V.; Leonova, V.A. *Mica-Bearing Pegmatites of Northern Karelia*; Nauka/Nedra: Leningrad, Russia, 1976; p. 367.
95. Shmakin, B.M. *Muscovite and Rare Metal*; Nauka/Novosibirsk: Leningrad, Russia, 1976, 376 p.
96. Michard, A.; Saddiqi, O.; Chalouan, A.; Frizon de Lamotte, D. *Continental Evolution: The Geology of Morocco*, 1st ed.; Springer: Berlin/Heidelberg, Germany, 2008; pp. 1–426.
97. Essaifi, A.; Samson, S.; Goodenough, K. Geochemical and Sr–Nd isotopic constraints on the petrogenesis and geodynamic significance of the Jebilet magmatism (Variscan Belt, Morocco). *Geol. Mag.* **2013**, *151*, 666–691.

Disclaimer/Publisher's Note: The statements, opinions and data contained in all publications are solely those of the individual author(s) and contributor(s) and not of MDPI and/or the editor(s). MDPI and/or the editor(s) disclaim responsibility for any injury to people or property resulting from any ideas, methods, instructions or products referred to in the content.